The Report Committee for Kit-Kwan Chiu
Certifies that this is the approved version of the following report:

Numerical Simulation Results for Problems 1, 2, 4, 6, and 7 of the Geothermal Code Comparison Study

APPROVED BY
SUPERVISING COMMITTEE:

Supervisor:

Mark McClure

Nicolas Espinoza

Numerical Simulation Results for Problems 1, 2, 4, 6, and 7 of the Geothermal Code Comparison Study

by

Kit-Kwan Chiu, B.S., M.S.

Report

Presented to the Faculty of the Graduate School of

The University of Texas at Austin

in Partial Fulfillment

of the Requirements

for the Degree of

Master of Science in Engineering

The University of Texas at Austin

May 2015

Acknowledgements

I thank my advisor, Dr. Mark McClure, since this study could not be done without his guidance and support. I am also grateful to Dr. Nicolas Espinoza for his valuable comments as the second reader of this report.

I also thank the U. S. Department of Energy, Geothermal Technologies Office, for conducting this geothermal code comparison study. I am grateful to the organizer, Dr. Mark White, and to all the problem champions who assisted me through the process of solving the benchmark problems. In addition, thanks go to Jack Norbeck from Stanford University, who gave me many useful suggestions to clarify the problem setup.

I would also like to express my gratitude to Mohsen Babazadeh for supplying his newly implemented codes for the penny-shaped fracture setup in Problem 4 and the surface displacement observation in Problem 7. My thanks also go to Sogo Shiozawa for being such a great help when I encountered technical problems related to result visualization.

I thank my officemates Yiwei and Hojung; we have struggled together and supported each other during the past two years. Thank you to dear Hyungjoo for always being there even when I feel low.

Finally, I sincerely thank my family for their unconditional love and support.

Abstract

Numerical Simulation Results for Problems 1, 2, 4, 6, and 7 of the Geothermal Code Comparison Study

Kit-Kwan Chiu, M.S.E.

The University of Texas at Austin, 2015

Supervisor: Mark McClure

This report summarizes work done for a geothermal code comparison study (GTO-CCS) organized by the Geothermal Technologies Office. The project evaluated a wide range of numerical simulators by performing a series of benchmark problems. Numerical simulators for Enhanced Geothermal Systems (EGS) enable solution of problems related to coupled thermal (T), hydrologic (H), geomechanical (M), and geochemical (C) mechanisms. Our simulations in this study were performed using a discrete fracture network (DFN) simulator, Complex Fracturing ReseArch Code (CFRAC). Results of five comparison problems are presented in this report.

Problems 1, 6, and 7 are solved as H-M cases. Problem 1 is an effective continuum problem that uses a correlation between fluid pressure and permeability. Results are compared on the basis of time series and spatial distribution plots of pressure, permeability, and fluid density. Problem 6 investigates changes in aperture and shear

displacement along a fracture during injection. Also, normal and shear stress distributions are compared. Problem 7 examines the surface vertical displacement caused by injecting water into an extremely shallow fracture. In addition, the mode-I stress intensity factors along the fracture edges are calculated.

Problems 2 and 4 are T-H-M cases. Some groups included thermoelastic stresses, but we could not because of the limitations of CFRAC. Problem 2 investigates fluid pressure and thermal transport in either a DFN or a continuum approximation to a fractured medium. Problem 4, inspired by the first EGS site in the United States at Fenton Hill, New Mexico, involves a single fracture intercepted by an injection well and a production well. The simulated fluid injection pressure and production temperation are compared with measured field data.

This project shows that numerical simulation is a pragmatic tool to analyze the complexity of the fluid injection and deformation processes. Physical characteristics including fluid pressure, permeability, fracture deformation, flow rate, and temperature distribution can be calculated and provide a clearer picture of a geothermal reservoir.

Table of Contents

List of Tables

List of Figures

Chapter 1: Introduction

This report discusses the first-stage results of our team, UT Austin, which participated in a geothermal code comparison study conducted by the U. S. Department of Energy Geothermal Technologies Office in 2014.

Geothermal energy is a promising energy source that can help meet the future energy needs of the United States. Conventional geothermal reservoirs (hydrothermal reservoirs) have a combination of heat, permeable rocks, and hot water which can be produced by wells to the surface for generating electricity (U.S. Department of Energy 2008). However, it is difficult to find places where heat, permeability, and water coexist. Thus, in order to increase production from geothermal energy, the "Enhanced Geothermal Systems" (EGS) technique has been developed to improve formation permeability in geothermal reservoirs (McClure 2014a). EGS projects can be pursued at sites that have sufficient temperature, regardless of natural permeability.

Enhanced Geothermal Systems involve drilling wells into hot rock, fracturing the rock to increase its permeability, and then circulating fluids to extract the heat from the reservoir. Cold fluid is injected into the reservoir via an injection well. While the fluid flows through the fractures, the fluid is heated by the surrounding formation. After the fluid has reached the production well, the heat can be extracted to generate electricity via turbines on the surface. The water is re-injected into the reservoir to maintain pressure.

Numerical simulation is used to investigate thermal, hydrological, geomechanical, and geochemical (T-H-M-C) processes. Geothermal systems can be considered natural heat exchangers, which allow fluid to flow through fractures and exchange heat with surrounding rocks (Deb and Jenny 2015). Hydrologic mass transport should be taken into account because the injected fluid migrates through fractures within the reservoir.

Injected fluid can influence the in-situ stress field. Finally, the injected fluid can cause geochemical reactions with the surrounding rocks, such as dissolution and precipitation. By applying numerical simulation, we can predict reservoir variables such as pressure, permeability, and temperature, which is essential for designing EGS projects.

In 2014, the Department of Energy (DOE) Geothermal Technologies Office organized a project, the geothermal code comparison study (GTO-CCS), to evaluate preexisting numerical simulators developed by diverse research groups by solving a series of key problems related to EGS. The comparison was set up to distinguish the effectiveness and accuracy of the different codes for EGS modeling. The twelve participating teams, members, and their codes are listed by White and Phillips (2015). The code comparison study has two phases: benchmark problems and challenge problems. By the end of 2014, seven benchmark problems (**Table 1**) for the first stage had been selected, solved, and fully discussed by the twelve teams from universities, national laboratories, and industry. In the second stage, in mid-2015, solving the challenge problems will focus on matching field-scale observational data (White and Phillips 2015).

In the GTO-CCS project, our UT Austin team was the problem champion of Problem 3. That work was done by Mark McClure and presented in Ghassemi et al. (2015) and so is not included in this report. We also provided results for Problems 1, 2, 4, 6, and 7. The only problem we were unable to solve is Problem 5. It is the only problem that required geochemical modeling, and the code we use, CFRAC, has not been equipped with this functionality. In this report, our solutions of Problems 1, 2, 4, 6, and 7 are presented.

Table 1: Benchmark problems and the corresponding problem champions. For the class type key, T: thermal energy transport, H: hydrologic mass transport, M: geomechanics, and C: geochemistry (White and Phillips 2015)

Problem	Title	Class Type	Problem Champion
1	Poroelastic response in a fault zone (Permeability-pressure feedback)	H-M/ T-H-M	Robert Podgorney, Idaho National Laboratory
2	Shear stimulation of randomly oriented fractures via pore pressure increase and thermal stress	T-H-M	Sharad Kelkar, Los Alamos National Laboratory
3	Fracture opening and sliding in response to fluid injection	H-M	Mark McClure, The University of Texas at Austin
4	Planar EGS fracture of constant, penny-shaped aperture in permeable hot rock	T-H/ T-H-M	George Danko, The University of Nevada at Reno
5	Amorphous silica dissolution/ precipitation in a fracture zone	T-H-C	Mark White, Pacific Northwest National Laboratory
6	Injection into a fault/fracture in thermo-poroelastic rock	H-M/ T-H-M	Ahmad Ghassemi, The University of Oklahoma
7	Surface deformation from a pressurized subsurface fracture	H-M	Pengcheng Fu, Lawrence Livermore National Laboratory

Chapter 2: Methodology

Our simulations are performed using a discrete fracture network (DFN) simulator called the Complex Fracturing ReseArch Code (CFRAC). The original two-dimensional version of CFRAC was developed by McClure and Horn (2010, 2014a) and was extended to 3D by McClure et al. (2015).

This chapter summarizes the main characteristics and basic equations of CFRAC. CFRAC calculates fluid flow and deformation along individual fractures, either pre-existing or newly forming fractures. For the pre-existing fractures, the location and orientation can be defined manually by the user or can be generated stochastically. For the potentially forming fractures, the location and orientation have to be prespecified by the user or by a specialized algorithm in the code.

2.1 BASIC EQUATIONS

In CFRAC, the fluid is single phase, single component, and isothermal (McClure 2012; McClure and Horn 2013). Fluid flow is simulated using the unsteady state mass balance equation (2.1) with the assumption of Darcy flow (eq. 2.2):

$$\frac{\partial(\rho E)}{\partial t} = -\nabla \cdot (q_{flux} e) + s \,, \tag{2.1}$$

and

$$q_{flux} = -\frac{k\rho}{\mu} \nabla P \,, \tag{2.2}$$

where, ρ is fluid density, E is the void aperture of the fracture, t is time, e is the hydraulic aperture for the fluid flow, s is a source term, q_{flux} is the mass flux of fluid, k is permeability of the fracture defined by equation (2.3):

$$k = \frac{e^2}{12}, \tag{2.3}$$

where, μ is fluid viscosity, and P is fluid pressure. The transmissivity of the fracture is equal to the product of permeability and hydraulic fracture as equation (2.4):

$$T = ke = \frac{e^3}{12}. \tag{2.4}$$

Two methods are available for calculating fluid viscosity. In one method, viscosity and fluid viscosity are assumed constant. Density is calculated as a function of pressure using the equation (2.5):

$$\rho = \rho_0 \cdot \exp((P - P_0)c_w), \tag{2.5}$$

where, ρ_0 is the initial fluid density, P_0 is the initial fluid pressure, and c_w is the fluid compressibility.

In the second method, viscosity and density are functions of both pressure and temperature. Lookup tables are used to calculate the fluid properties. Tables are available for water, CO_2, and N_2. The data in the tables are taken from "Thermophysical Properties of Fluid Systems" in the NIST Chemistry WebBook (Lemmon et al. 2015).

Fracture elements are either closed or open in CFRAC. When the fluid pressure is less than the normal stress on the fracture, the fracture is closed, and its walls remain in contact. Due to the roughness of the walls of the fracture, fluid can be stored and conduct through fractures that are mechanically closed. For a closed fracture element, Coulomb's

failure criterion (eq. 2.6) is used to determine whether this element should slip. CFRAC calculates the void aperture (the pore volume per unit area), E, and the hydraulic aperture (the effective aperture for fluid flow), e, with equations (2.8) and (2.9), respectively. The void aperture should always be larger than or equal to the hydraulic aperture.

$$| \tau - \eta v | = \mu_f \sigma_n^{'} + S_0 , \tag{2.6}$$

$$\sigma_n^{'} = \sigma_n - P , \tag{2.7}$$

$$E = \frac{E_0}{1 + \frac{9\sigma_n^{'}}{\sigma_{n,Eref}}} , \tag{2.8}$$

and

$$\mathrm{e} = \frac{e_0}{1 + \frac{9\sigma_n^{'}}{\sigma_{n,eref}}} + D_{\mathrm{e},eff} \tan \frac{\varphi_{edil}}{1 + \frac{9\sigma_n^{'}}{\sigma_{n,eref}}} , \tag{2.9}$$

where, τ is the shear stress, η is a radiation damping parameter defined as $G/(2v_s)$ where G is the shear modulus and v_s is the shear wave velocity, v is the slip velocity (Rice 1993), μ_f is the coefficient of friction, σ_n' is the effective normal stress defined by equation (2.7), σ_n is the normal stress, P is the fluid pressure in the fracture, S_0 is the cohesion of the fracture, E_0 and e_0 are the void and hydraulic apertures at zero effective normal stress, $\sigma_{n,Eref}$ and $\sigma_{n,eref}$ are the reference closure stress, also known as the required normal stress for a 90% reduction of void and hydraulic apertures, φ_{edil} is the shear dilation angle corresponding to the transmissivity of the fracture, and $D_{\mathrm{e},eff}$ is the cumulative shear displacement (up to a maximum value, $D_{e,eff,max}$).

When the fluid pressure reaches the normal stress, the fracture opens and the walls are no longer in contact. The effective normal and shear stress on the fracture surface is enforced to equal zero. CFRAC calculates the void aperture and the hydraulic aperture of open fracture elements using equations (2.10) and (2.11):

$$E = E_0 + D_{E,eff} \cdot \tan\varphi_{Edil} + E_{open}, \tag{2.10}$$

and

$$e = e_0 + D_{e,eff} \cdot \tan\varphi_{edil} + E_{open}, \tag{2.11}$$

where E_{open} is the mechanical separation between the fracture walls.

2.2 FLUID LEAKOFF

The fluid leakoff from the fracture surface into the surrounding matrix is calculated by adding the mass rate of leakoff, $q_{leakoff}$, into equation (2.1):

$$\frac{\partial(\rho E)}{\partial t} = -\nabla \cdot \left(q_{flux} e\right) - q_{leakoff} + \mathrm{s}. \tag{2.12}$$

In CFRAC, there are two options for modeling leakoff. One option is to use the 1D leakoff model developed by Vinsome and Westerveld (1980), which accounts for changing pressure in the fracture over time, but does not account for interference from neighboring fractures (McClure et al. 2015). The 1D leakoff model also assumes single-phase flow, constant formation permeability, fluid compressibility, fluid viscosity, and matrix porosity compressibility and neglects poroelastic effects in the matrix.

Leakoff can also be calculated fully numerically. This option simulates fluid flow in both the matrix and the fracture by using an unstructured mesh, as described by McClure (2014b).

2.3 THERMAL TRANSPORT

Another newly implemented option in CFRAC is thermal transport (McClure and Horne 2014b), which models heat transport from both conduction and convection. Thermal transport can be calculated implicitly with the Crank-Nicolson time stepping method or implicit Euler method. In the matrix, thermal transport can be calculated using the 1D Vinsome and Westerveld (1980) method or fully numerically with an unstructured grid.

Thermal transport can be simulated using an energy balance equation. Equation (2.13) is the integral form of the governing equation of thermal transport in a porous media, neglecting radiation.

$$\frac{\partial}{\partial t}\int_{V_n}\left[\sum_{\gamma=l,g}\left(\phi\rho_\gamma s_\gamma u_\gamma\right)+\left(\left(1-\phi\right)\rho_r u_r\right)\right]dV_n=\int_{\Gamma_n}\left[E\times n\right]d\Gamma_n+\int_{V_n}\left[\sum_{\gamma=l,g}\left(h_\gamma m_\gamma\right)+q_e\right]dV_n, \quad (2.13)$$

where t is time, V_n is the volume, φ is the porosity, ρ_γ is the fluid density, s_γ is the fluid saturation, u_γ is the fluid internal energy, ρ_r is the rock density, u_r is the rock internal energy, E is the energy flux tensor, n is the unit surface normal vector, Γ_n is the volume surface area, h_γ is the fluid enthalpy, m_γ is the mass flow rate entering the volume, and q_e is the thermal energy source entering the volume. The energy flux, E, can be calculated by equation (2.14):

$$E = -\nabla\left(k_e \nabla \mathrm{T}\right) + \sum_{\gamma=l,g}\left(\rho_\gamma h_\gamma V_\gamma\right), \tag{2.14}$$

where k_e is the effective thermal conductivity tensor, T is temperature, and V_γ is the fluid flux tensor volume calculated by equation (2.15):

$$V_\gamma = -\frac{k_{r\gamma} k}{\mu_\gamma}\left(\nabla P_\gamma + \rho_\gamma g z\right), \tag{2.15}$$

where $k_{r\gamma}$ is the relative permeability of the fluid, k is the intrinsic oermeability tensor, μ_γ is the fluid viscosity, P_γ is the fluid pressure, g is the acceleration of gravity, and z is the gravitational unit vector. In the simulations we performed, gravity was neglected.

Chapter 3: Benchmark Problem 1

3.1 PROBLEM OVERVIEW AND DESCRIPTION

The problem geometry is a 4-m thick horizontal fault zone. The fault zone is located at depth of 2000 m and is surrounded by dense basalt with lower permeability than in the fault zone. It is a simple radial flow problem, and the simulated quarter matrix is set as 2000 m x 2000 m x 4 m. Constant injection rate, initial and constant boundary conditions, maximum simulation time, and fault zone properties are specified according to the problem statement. Simulations with leakoff and without leakoff into the surrounding basalt are performed.

3.2 SYSTEM CONFIGURATION

As shown in **Figure 1a**, water is injected into a permeable fault zone from a 0.15 m radius wellbore. This problem can be approached with a symmetry solution. A 1/8 symmetric domain of the fault zone is shown in Cartesian coordinates in **Figure 1b**. The length and width of the domain are set to 2000 m. An unstructured triangle mesh of the fault zone is created by CFRAC (**Figure 2a**), the size of each triangle decreasing closer to the wellbore. CFRAC only permits the well to be a line, but the problem description defines a circular wellbore. In order to be similar to the circular wellbore with a diameter of 0.3 m specified in the problem, the dimension of the quarter wellbore has been modified to be a triangle, as shown in **Figure 2b**.

Permeability of the fault zone follows an exponential law as a function of stress as defined by Nathenson (1999):

$$k = k_0 \cdot \exp(\frac{cdP}{\sigma}), \tag{3.1}$$

where k_0 is the permeability at zero fluid pressure, c is a fitting parameter, σ is the total overburden confining stress (the normal stress on the horizontal fault zone), and dP represents the variation of fluid pressure from the initial state. In this problem, k_0 is set as 10^{-13} m^2, the fitting parameter is 10, and the overburden confining stress is 45 MPa.

The density of water is a function of pressure calculated by equation (3.2):

$$\rho = \rho_0 \cdot \exp(c_w(P - P_o)), \tag{3.2}$$

where the initial water density (ρ_0), water compressibility (c_w), and initial pressure (P_0) are given in **Table 2**.

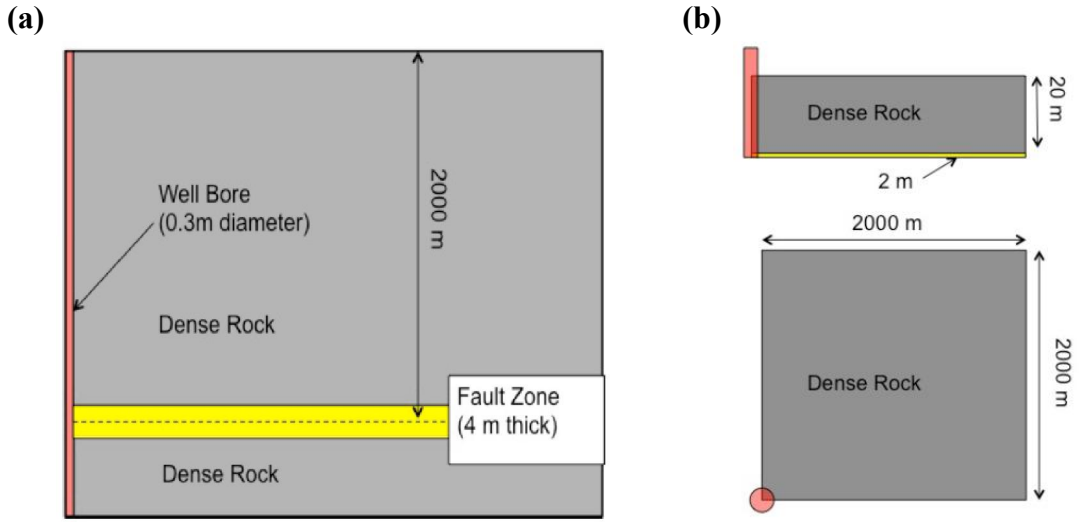

Figure 1: **(a)** Geometry of Problem 1, **(b)** 1/8 symmetric mesh in Cartesian coordinates (Bahrami et al. 2015)

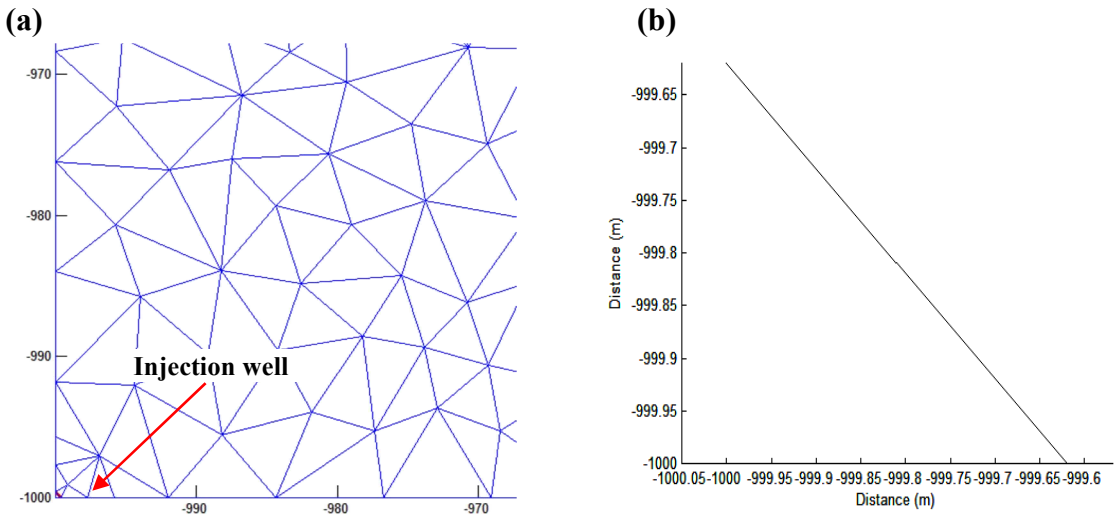

Figure 2: **(a)** Triangle mesh of the fault zone, **(b)** Wellbore arrangement

Table 2: Input properties of Problem 1

Property	Value		Unit
	Fault zone	Dense basalt	
Permeability	$1 \cdot 10^{-13}$	$1 \cdot 10^{-18}$	m^2
Porosity	$1 \cdot 10^{-4}$	$1 \cdot 10^{-2}$	
Pore compressibility	$1 \cdot 10^{-7}$	$4 \cdot 10^{-10}$	Pa^{-1}
Water density	936.42		kg/m^3
Water viscosity	$2.0151 \cdot 10^{-4}$		Pa·s
Water compressibility	$4.475 \cdot 10^{-10}$		Pa^{-1}
Injection rate	80		kg/s
Initial fluid pressure	20		MPa
Compressive stress in x-dir.	50		MPa
Compressive stress in y-dir.	50		MPa
Remote shear stress	0		MPa
Simulation duration	259200		s

3.3 INITIAL AND BOUNDARY CONDITIONS

For simulating water injection into the entire fault zone, we divide the fault zone into four quarters and keep the thickness at 4 m. The injection flow rate therefore becomes a quarter of the total flow rate, 20 kg/s. The lower and left sides of the mesh domain are treated as no-flow boundaries; the right and upper sides are set as constant pressure boundaries with the value of the initial fluid pressure. Other properties of the fault zone and the surrounding dense rock are given in **Table 2**.

For the top and bottom of the fault zone (the out-of-plane boundaries), two different treatments are used. In the "no-leakoff" case, it is assumed that the out-of-plane boundaries are no-flow boundaries. In the "leakoff" case, it is assumed that fluid can leak out of these out-of-plane boundaries into the surrounding basalt. To handle the leakoff in CFRAC, the Vinsome and Westerveld (1980) method is used. This is unusual in CFRAC, because typically the Vinsome and Westerveld (1980) method is used to model leakoff from discrete fractures into the surrounding matrix (within the same plane). In this case, the method is used to model out-of-plane leakoff from triangular continuum elements into the region overlaying and underlaying the problem domain.

3.4 METRICS

Time series at specified locations and a spatial distribution plot at 10000 seconds of pressure, permeability, and water density are provided (**Table 3**).

Table 3: Result metrics of Problem 1

Metric	Parameter	Locations (x, y, z) [m]	Time [s]
Time series	*Pressure* *Permeability* *Water density*	(1,1,2000), (2.5,2.5,2000), (5,5,2000), (10,10,2000), (50,50,2000), (500,500,2000),	Continuous
Spatial distribution	*Pressure* *Permeability* *Water density*	At x = y = 2000	10000

3.5 RESULTS

3.5.1 Time series

Six points in the fault zone are monitored: (1, 1), (2.5, 2.5), (5, 5), (10, 10), (50, 50), and (500, 500). Results of pressure, permeability, and water density versus time for both the leakoff and no leakoff cases are presented in **Figure 3**. The simulation duration is 259200 seconds.

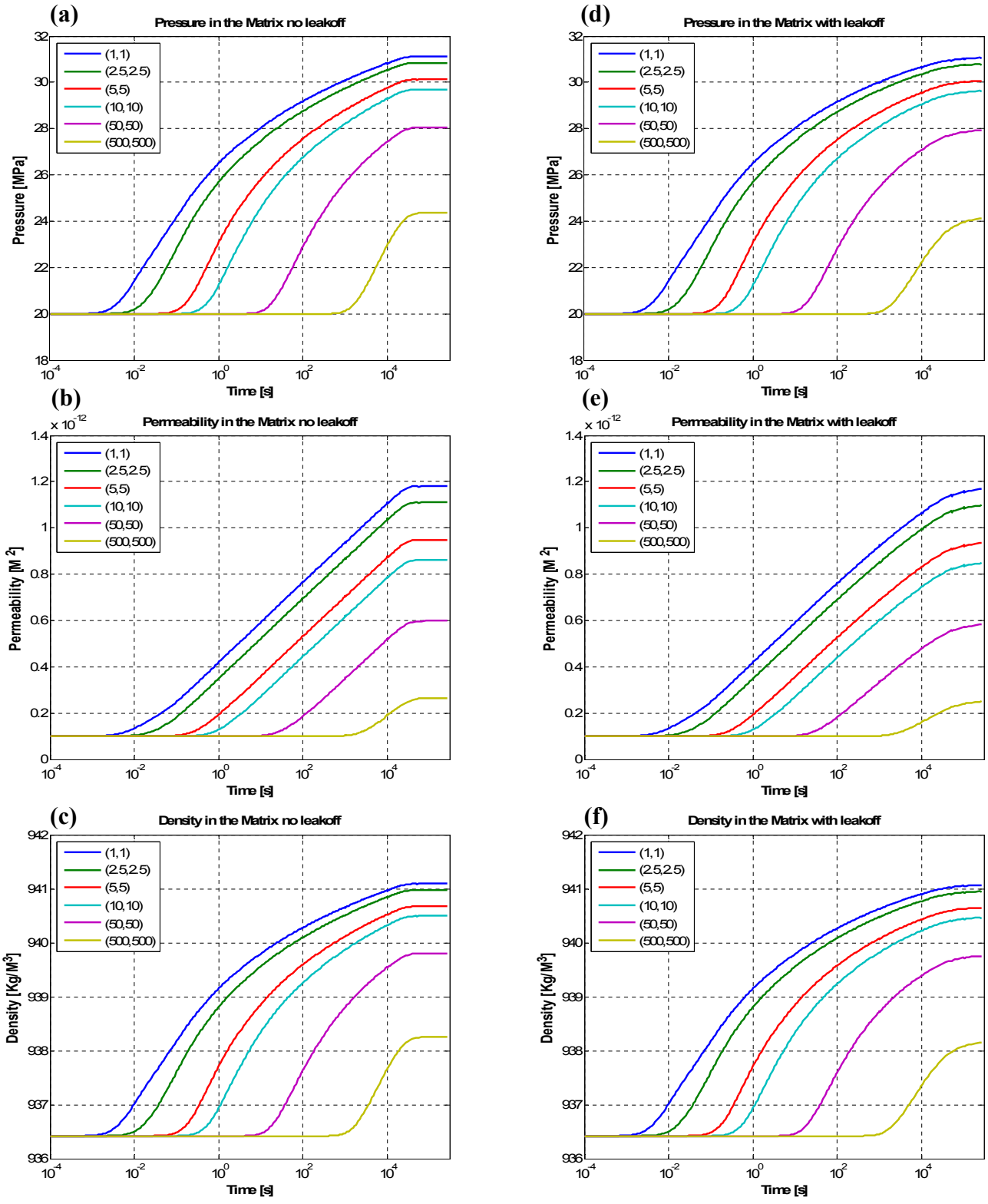

Figure 3: Time series of no leakoff and leakoff cases, from 0 to 259,200 s. **(a)**, **(b)**, **(c)** are the pressure, permeability, and water density results of the no leakoff case; **(d)**, **(e)**, and **(f)** are results of the leakoff case

3.5.2 Spatial distribution plot

The spatial distributions of pressure, permeability, and water density along x = y 2000 m at 10000 seconds are shown in **Figure 4**, where the x-axis refers to the distance from the wellbore (0, 0) to the margin of the domain (2000, 2000).

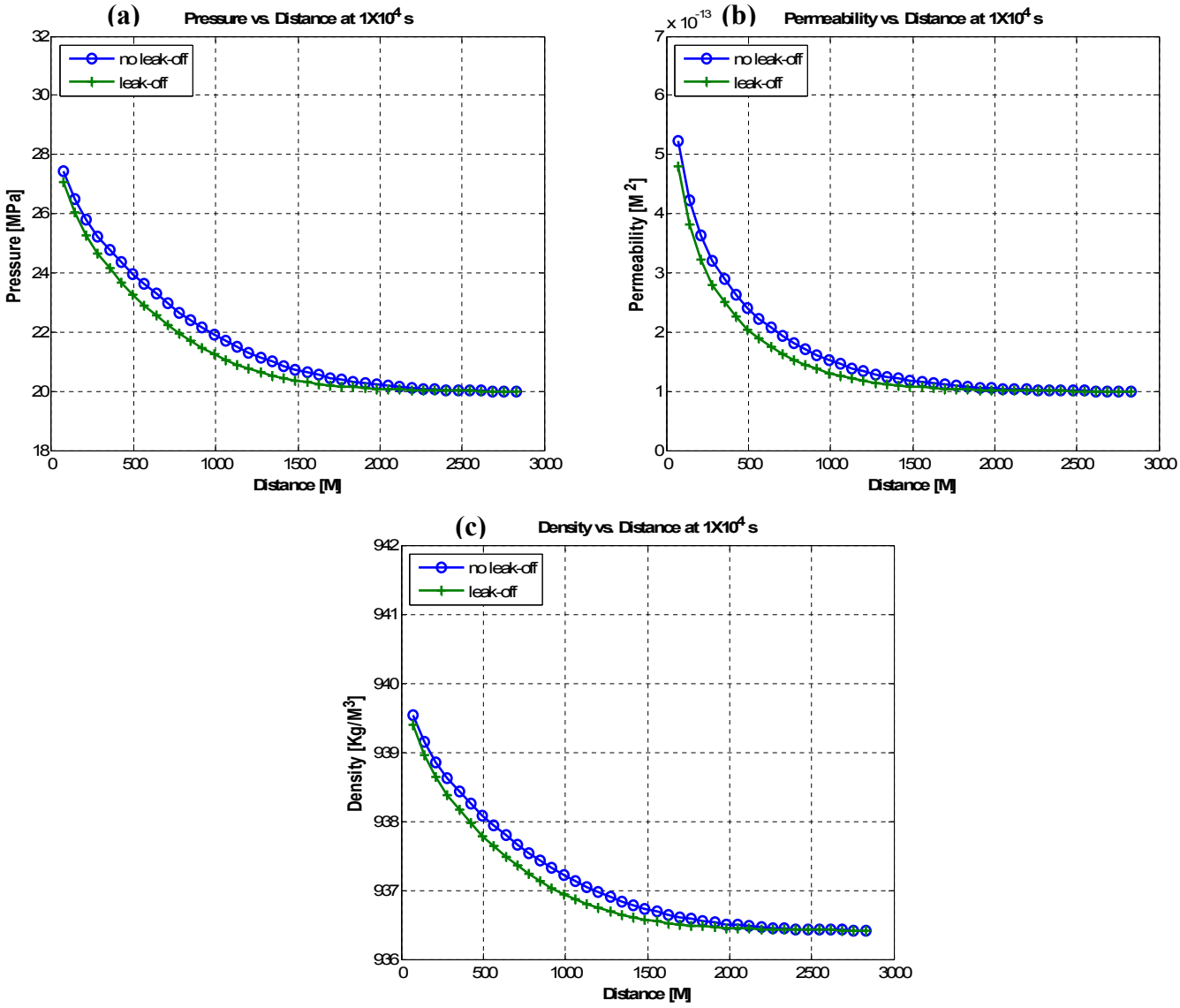

Figure 4: Spatial distribution of **(a)** pressure, **(b)** permeability, and **(c)** water density for no leakoff and leakoff cases from wellbore to 2828.43 m

3.6 REMARKS

The increase in fluid pressure leads to the increase of fracture permeability. The time series from the no leakoff case at the six different locations all reach steady state after 10^4 seconds. The highest values appear at the observation point near the wellbore as expected, around 31.02 MPa, $1.16 \cdot 10^{-12}$ m^2, and 941.15 kg/s, respectively. In the leakoff case, steady state is never reached, and the curves are smoother than in the no leakoff case. For the spatial distribution, both the pressure and permeability of the leakoff case are lower than the no leakoff case until 2000 m, where the effect of constant pressure boundary becomes more significant. Overall trends of both the time series and spatial distributions in the leakoff case are similar to those of the no leakoff case, just with slightly lower values.

Results from all the participating teams reached agreement for this problem (White and Phillips 2015). Therefore, this basic problem can serve as a baseline for future comparison.

Chapter 4: Benchmark Problem 2

4.1 Problem overview and description

This problem involves cold water injection at a point source at the center of a three-dimensional domain. The initial pressure, temperature, and stresses are fixed at the boundary. Several fundamental concepts are taken into account, such as poro-thermoelastic effects due to changes in pressure and temperature and shear stimulation of natural fractures.

CFRAC is unable to fully solve the benchmark problem. Poro-thermoelastic responses are neglected in CFRAC, and the wellbore setting in CFRAC is always assumed to be a linear shape, which does not satisfy the point source setting in this problem. Also, the problem involved a three-dimensional problem domain, but CFRAC can only model continuums in a two-dimensional problem domain. Although CFRAC cannot be used to simulate this problem exactly, we nevertheless used CFRAC to simulate the problem as much as possible.

4.2 System configuration

The problem geometry is shown as **Figure 5**. The injection point is located in the center of the model domain. Because CFRAC can only model continuums in 2D, we set the problem up as a line source at the center of a two-dimensional (x-z) domain as a horizontal well. Three different problem setups were used: a less dense DFN (**Figure 6a**), a very dense DFN (**Figure 6b**), and a full-continuum domain that does not contain any fractures (**Figure 6c**).

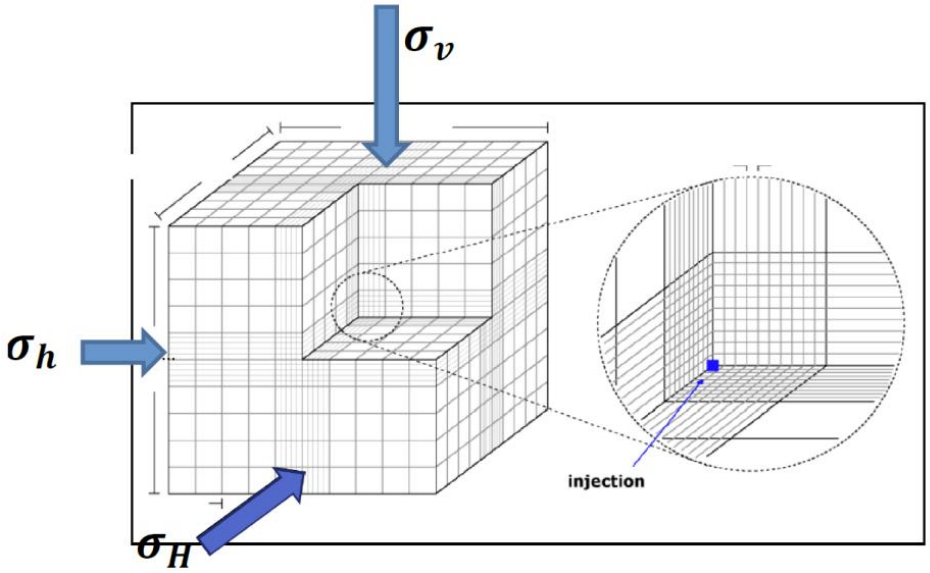

Figure 5: Geometry of the model domain showing the injection point at the center (adapted from the problem description)

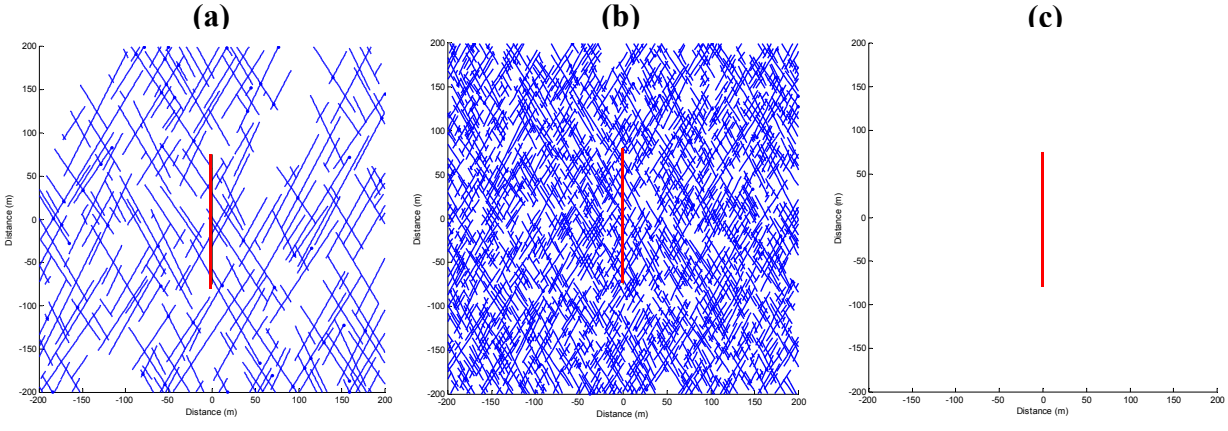

Figure 6: Three domain settings: **(a)** very dense DFN, **(b)** less dense DFN, and **(c)** full continuum. Wellbores are the red lines at the center

Four governing equations are involved during the process (Ghassemi et al. 2015): (1) Darcy's law of single-phase water flow; (2) heat balance, including advection and conduction; (3) static force balance with linear elasticity, including pore pressure and thermal effects, and small strain; and (4) the Mohr-Coulomb criterion for shear failure:

$$MCStress \equiv \frac{1}{2}\left(\sigma_1 - \sigma_3\right)\left(\mu^2 + 1\right)^{\frac{1}{2}} - \frac{1}{2}\mu\left(\sigma_1 + \sigma_3\right) + \mu P - S_0, \tag{4.1}$$

where σ_1 and σ_3 are the maximum and minimum principal stresses, μ is the coefficient of friction, P is the pore pressure, and S_0 is the cohesion.

Matrix permeability is calculated using equations (4.2) to (4.4) (Ghassemi et al. 2015), where $k_{initial}$ is the initial permeability, k_{max} is the maximum allowed permeability, and MC_{ramp} is the ramp stress - the value of MCStress when k_{max} is reached. The permeability as a function of Mohr-Coulomb stress is shown in **Figure 7**. In our work, equations (4.2) to (4.4) for calculating the permeability in the matrix were only applied in the full-continuum simulation which does not contain any fractures (**Figure 6c**).

$$k = k_{initial}, \text{ if } MCStress < 0, \tag{4.2}$$

$$k = k_{initial} + \left(\frac{MCStress}{MC_{ramp}}\right)\cdot\left(k_{max} - k_{initial}\right), \text{ if } 0 < MCStress \le MC_{ramp}, \tag{4.3}$$

$$k = k_{max}, \text{ if } MCStress < MC_{ramp}, \tag{4.4}$$

where $k_{max} = 55k_{initial}$ and $MC_{ramp} = 15\ [MPa]$.

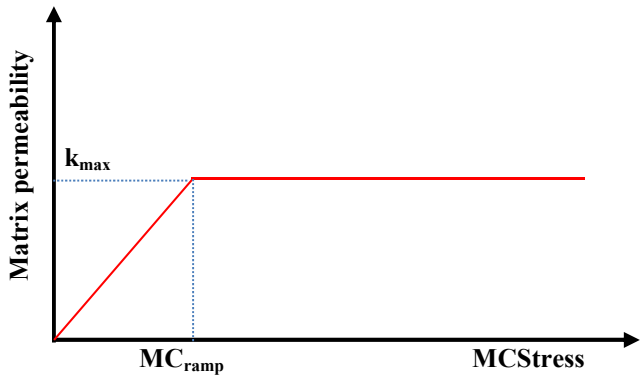

Figure 7: Matrix permeability as a function of Mohr-Coulomb stress (adapted from the problem description)

4.3 INITIAL AND BOUNDARY CONDITIONS

Initially, the reservoir is fully saturated by water with the pore pressure at 9.81 MPa and the temperature at 190^0C. External boundary conditions are (1) constant pore pressure equal to 9.81 MPa; and (2) no heat flow conduction (though energy could convect out of the model through the flowing fluid). The two-dimensional domain is in the x-z plane (400 m x 400 m) with a formation thickness of 100 m. The remote compressive stress is 13.88 MPa in the x-direction and 22.7 MPa in the z-direction. The duration of simulation is set to 27 days = 2332800 seconds. A vertical well interval is assigned from (0, -75) to (0, 75). Other properties of the domain are given in **Table 4**.

Table 4: Input Properties of Problem 2

Parameter		Value	Unit
Initial pore pressure		9.81	MPa
Reservoir temperature		190	^{0}C
Porosity		0.1	
Initial permeability, $k_{initial}$	*Case 4*	$2.6 \cdot 10^{-15}$	m^2
	The others	$2.6 \cdot 10^{-17}$	
Injection pressure		12.91	MPa
Injection temperature		100	^{0}C
Thermal conductivity		2.2	$W \cdot m^{-1} \cdot K^{-1}$
Rock density		2480	$kg \cdot m^{-3}$
Specific heat capacity		1200	$J \cdot m^{-3} \cdot K^{-1}$
Young's modulus		25	GPa
Poisson's ratio		0.2	
Mohr-Coulomb cohesion, S_0		3.0	MPa
Static friction coefficient, μ		0.6	
Compressive stress in x-dir.		13.88	MPa
Compressive stress in y-dir.		22.7	MPa
Remote shear stress		0	MPa
Simulation duration		2332800	s

4.4 RESULTS

Four different cases are simulated for this problem. Case 1 simulates the pressure and temperature distribution in the less dense DFN with a fully numerical solution for fluid flow and heat transport in the matrix. The fluid pressure distribution (**Figure 8a**) of the fractures changes from blue to red; the green to yellow range indicates the pressure distribution of the matrix, and the black line is the wellbore at the center. The fluid temperature distribution (**Figure 8b**) of the fractures also changes from red to blue, and the yellow-gold in the matrix shows the temperature of the matrix, which remains nearly constant except very close to the wellbore and the fractures. For providing a clearer view, the temperature distribution is zoomed in so that only the center part of the domain is shown.

Case 2 (**Figure 9**) also uses the less dense DFN. However, in this case, the 1D leakoff approximation is used to simulate leakoff, rather than the fully numerical solution. Heat conduction from the fractures is also treated with the Vinsome and Westerveld (1980) method.

Case 3 (**Figure 10**) uses the 1D leakoff/conduction approximation, but with a very dense DFN. Finally, Case 4, which is the only case calculating the matrix permeability using equation (4.2) to (4.4), shows the results of a full-continuum simulation (**Figure 11**).

Injection flow rates versus time for the four cases are compared in **Figure 12**. Case 3 has the highest flow rate and is followed by Case 4, Case 2, and Case 1.

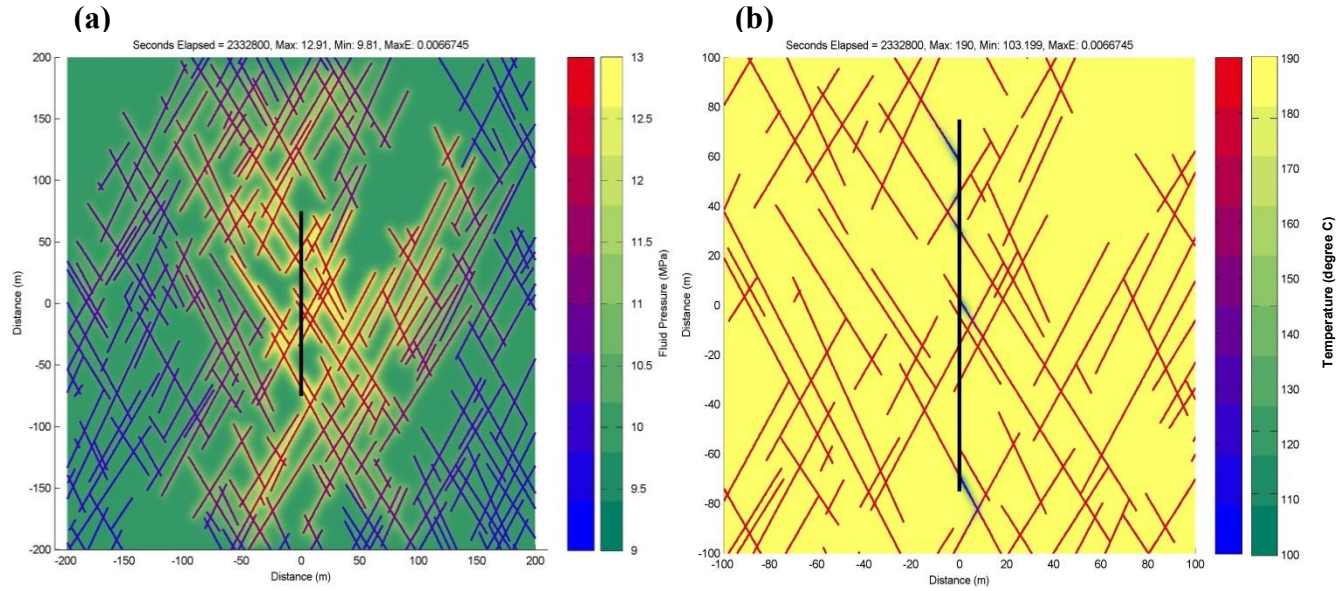

Figure 8: **(a)** Pressure and **(b)** temperature distribution of Case 1: less dense DFN, full solution

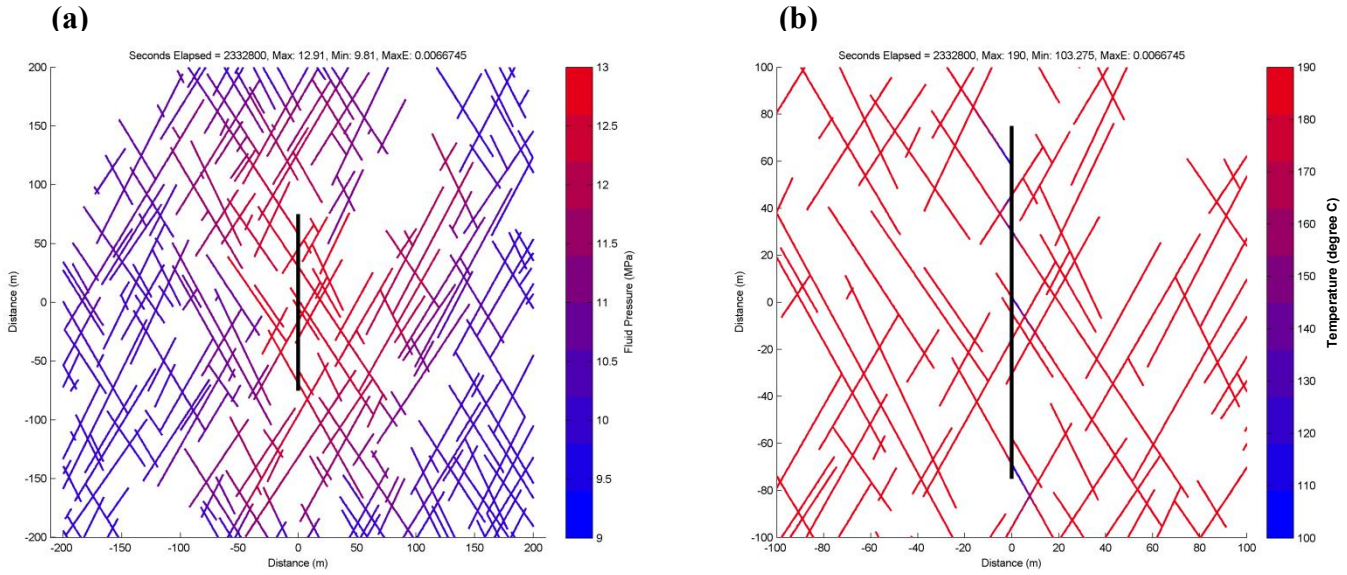

Figure 9: **(a)** Pressure and **(b)** temperature distribution of Case 2: less dense DFN with one-dimensional leakoff

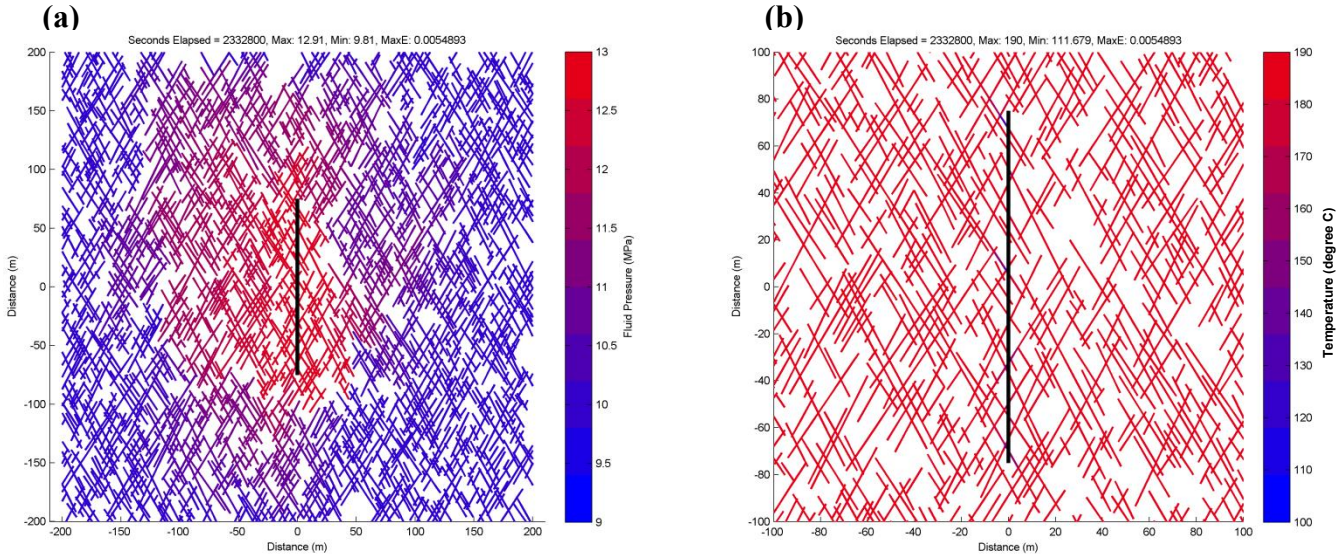

Figure 10: **(a)** Pressure and **(b)** temperature distribution of Case 3: very dense DFN with one-dimensional leakoff

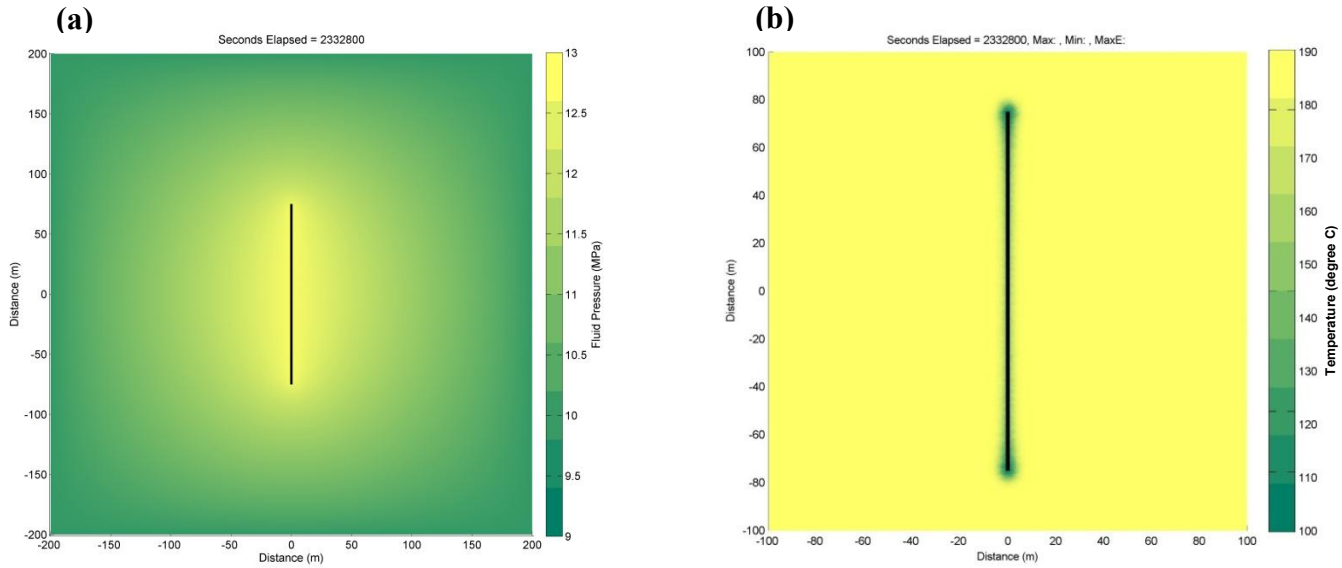

Figure 11: **(a)** Pressure and **(b)** temperature distribution of Case 4: a full-continuum matrix domain

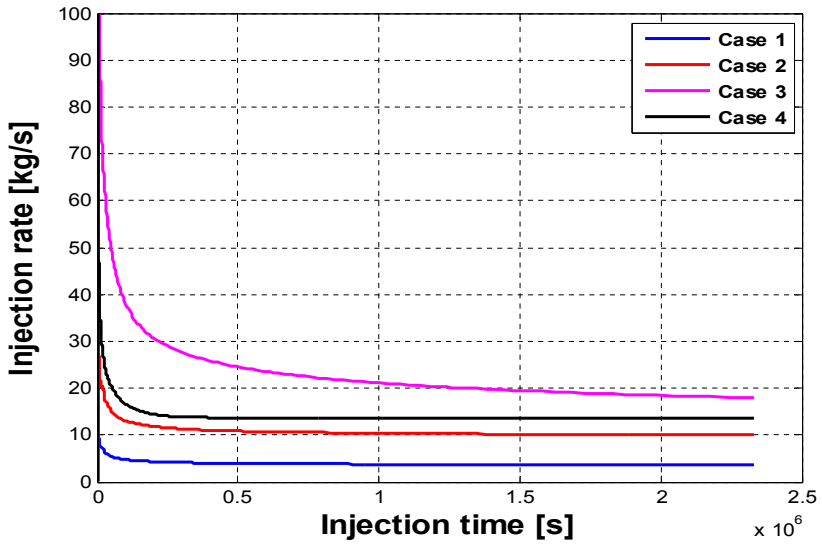

Figure 12: Flow rate versus time of the four cases from 0 to 2332800 s

4.5 REMARKS

In the results of Cases 1, 2, and 3, as the fluid pressure goes up; shear stimulation occurs to the fractures and causes the conductivity to increase. The pressure distribution is not uniform, so the pressure in some places is unchanged whereas in other places the pressure is very high. Similar to the pressure, the cooling is not uniformly distributed in the entire domain. Local temperature variation is observed at a very few places where the fractures are intercepting the wellbore and taking most of the flow.

Since the problem requires us to simulate permeability as a function of pressure, the results in Case 4 are supposed to be the most comparable ones to the point source setting in the problem description. If we compare the results of all the cases, the pressure front of the DFN cases extends further away from the well because the fluid is localized in a few fractures during the injection. On the contrary, due to the better sweep efficiency of the full-continuum case, the pressure front is more uniformly moving through the formation.

Thermal stress was negleted when solving this problem, but if we had included the thermal stress, the results would have been affected. Cool water injection would have caused the surrounding rock to shrink locally and introduced a more heterogeneous state of stress along the fracture (Norbeck and Horne 2015). The effective stress would have dropped at the injection site where the temperature was lower. As the temperature contrast between the water and the surrounding rock increased, the cooling-induced crack opening would have increased (Ghassemi et al 2015).

Chapter 5: Benchmark Problem 4

5.1 PROBLEM OVERVIEW AND DESCRIPTION

The objective of this problem is to simulate fluid circulation in a single fracture. This problem is very loosely based on the first experimental EGS in the U.S., at Fenton Hill, New Mexico. Two scenarios are tested: Case 1 and Case 2 (**Figure 13**). In Case 1, a penny-shaped, constant-aperture, circular fracture is assumed, and injection flow rate and temperature are given. The temperature and pressure loss across the fracture should be simulated by the thermal-hydrologic (T-H) model. In Case 2, a self-opening, circular fracture is assumed to be nearly closed before injection. Following basic rock mechanics, a fracture opens when the pore pressure exceeds the normal stress; therefore, Case 2 becomes a thermal-hydrologic-mechanical (T-H-M) model. Temperature and pressure across the fracture are simulated for a 75-day period. Temperature and pressure results of Case 1 and Case 2 will be compared with the published measured data of Fenton Hill (Murphy et al. 1981) to determine the more likely fracture geometry for simulating similar field cases in the future.

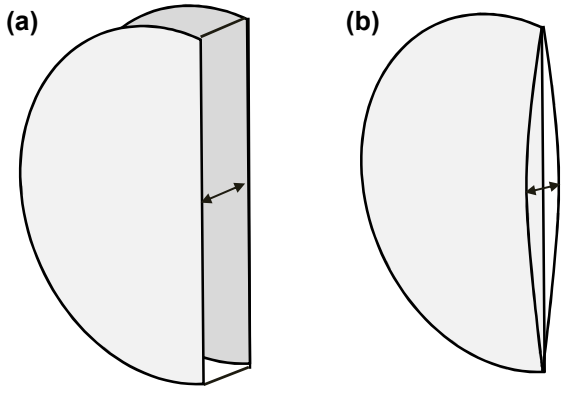

Figure 13: Fracture geometry. **(a)** Case 1: penny- shaped, constant aperture fracture, **(b)** Case 2: self-opening circular fracture (adapted from the problem description)

5.2 SYSTEM CONFIGURATION

A planar fracture at a specified depth sounded by impermeable rock is shown in **Figure 14**. The diameter of the circular fracture in both cases is assumed to be 120 m. Water is injected from the injection well at -2750 m and extracted from the production well at -2670 m.

In CFRAC, a penny-shaped fracture is set in the x-z plane (120 m·120 m), and the center is located at (0, 0, 0). The injection and production wells are located at (0, 0, -35) and (0, 0, 45), respectively. For Case 1, we set the fracture aperture as a constant (0.000141 m) and a very large normal stress (150 MPa) in the y-direction to prevent the fracture from opening. These are contrived values, chosen only to satisfy the problem specifications. For Case 2, we set the initial fracture aperture extremely small (0.000001 m), a setting in which the fracture can be considered nearly closed but will still allow a tiny amount of fluid to flow, and we set a smaller normal stress (37 MPa) in the y-direction. The fracture opens once the fluid pressure exceeds the normal stress on the fracture.

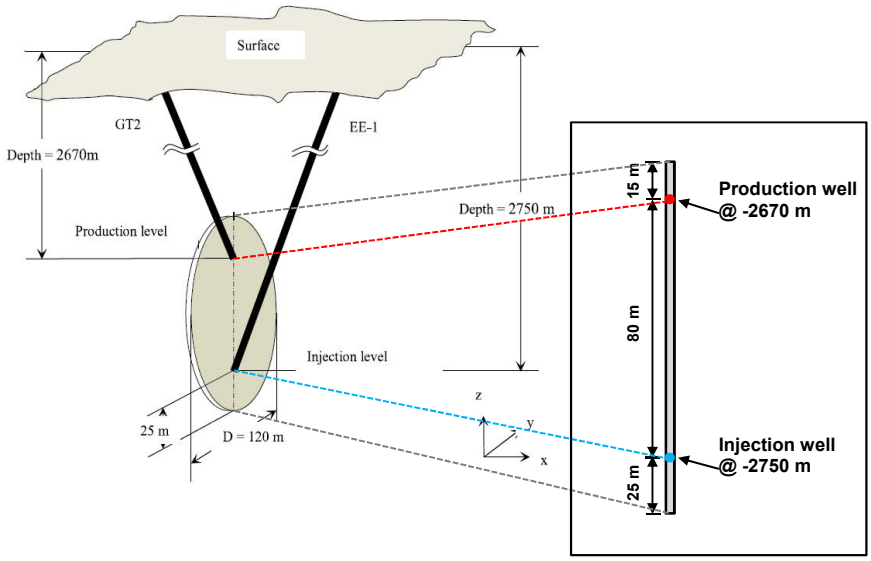

Figure 14: Reservoir and fracture schematic (Bahrami et al. 2015).

5.3 INITIAL AND BOUNDARY CONDITIONS

In all simulations, it is assumed that there is no fluid leakoff from the fracture. However, heat can conduct into the fracture from the surrounding matrix. This was handled in CFRAC using the 1D heat conduction approximation (Vinsome and Westerveld, 1980).

The temperature of the injection water at the surface is assumed to be 25^0C, but the water is heated when it reaches the bottom hole of the injection well due to the geothermal gradient. The temperature of water entering the fracture shown in **Figure 15** is a function of time that is explicitly specified to the simulator. The injection flow rate, specified in **Figure 16**, is 7.5 kg/s initially and then gradually increases to 15 kg/s from day 25 to day 35. After day 36, the flow rate is kept constant. Another boundary condition is that the pressure at the production well is assumed to be the same as the initial fluid pressure, 27.3 MPa, at all times. Other parameters set in CFRAC are given in **Table 5**.

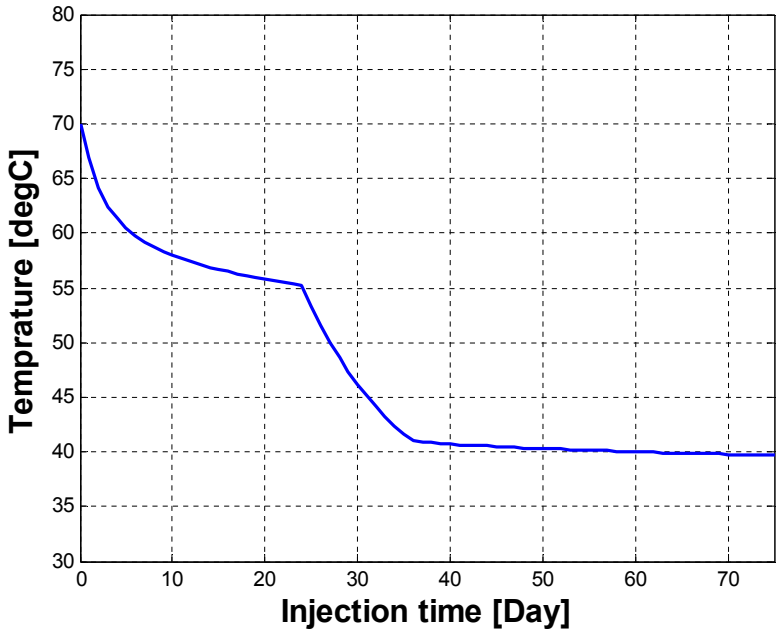

Figure 15: Temperature of coolant water at the injection site (adapted from the problem description)

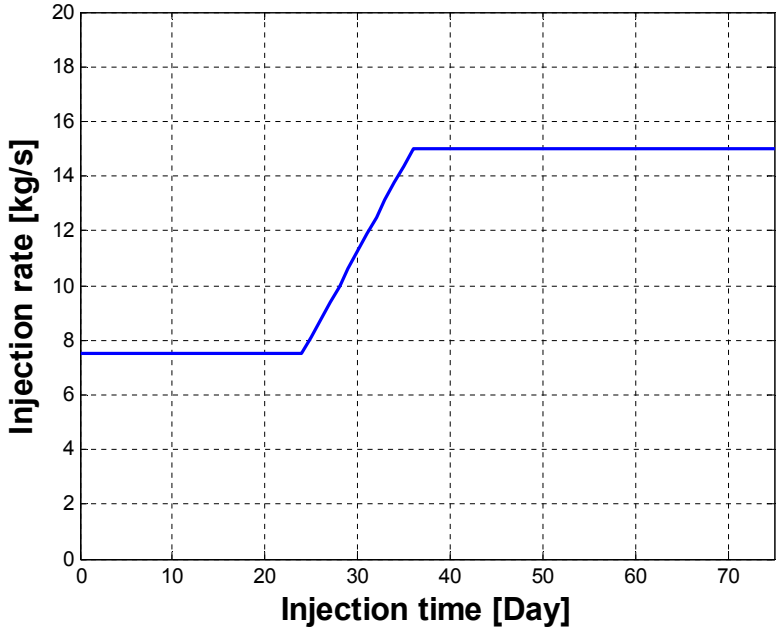

Figure 16: Injection rate for 75 days (adapted from the problem description)

Table 5: Input properties of Problem 4

Property	Value		Unit
	Case 1	**Case 2**	
Initial fluid pressure	27.3		MPa
Compressive stress in x-dir	37	100	MPa
Compressive stress in y-dir.	150	37	MPa
Remote shear stress	0		MPa
Initial aperture	0.000141	0.000001	m
Shear modulus	15		GPa
Poisson's ratio	0.25		
Simulation duration	6480000		s
Initial injection temperature	70		^{0}C
Initial temp. at the fracture center	183.075		^{0}C
Local geothermal gradient	55		^{0}C/km
Rock density	2700		kg/m^3
Thermal conductivity	2.9		W/m-K
Heat capacity	990		J/kg-K
Initial injection rate	7.5		kg/s
Fracture radius	60		m

5.4 METRICS

For both Case 1 and Case 2, times series of injection pressure and production temperature during the entire injection period are generated according to the settings given in **Table 6**.

Table 6: Result metrics of Problem 4

Metric	Parameter	Location (x, y, z) [m]	Time
Time series	*Pressure*	Injection site (0, 0, -2750)	75 days
	Temperature	Production site (0, 0, -2670)	

5.5 RESULTS

The time series of injection pressure and production temperature for both cases are shown in **Figure 17** and **Figure 18**, respectively. The measured data at Fenton Hill are estimated from the field data from the surface (Murphy, 1981).

Figure 19 and **Figure 20** present the distribution of pressure and temperature across the entire fracture for Case 1 and Case 2, respectively. In addition, the distributions of aperture and transmissivity of the fracture in Case 2 are shown in **Figure 20** because the aperture variation is the most distinct difference between these two cases.

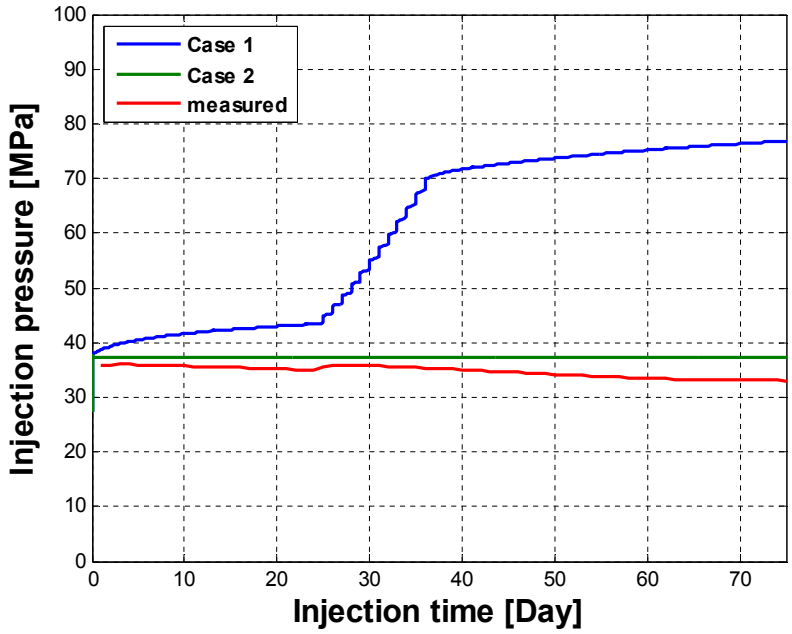

Figure 17: Injection pressure versus time for Case 1, Case 2, and the measured data at Fenton Hill

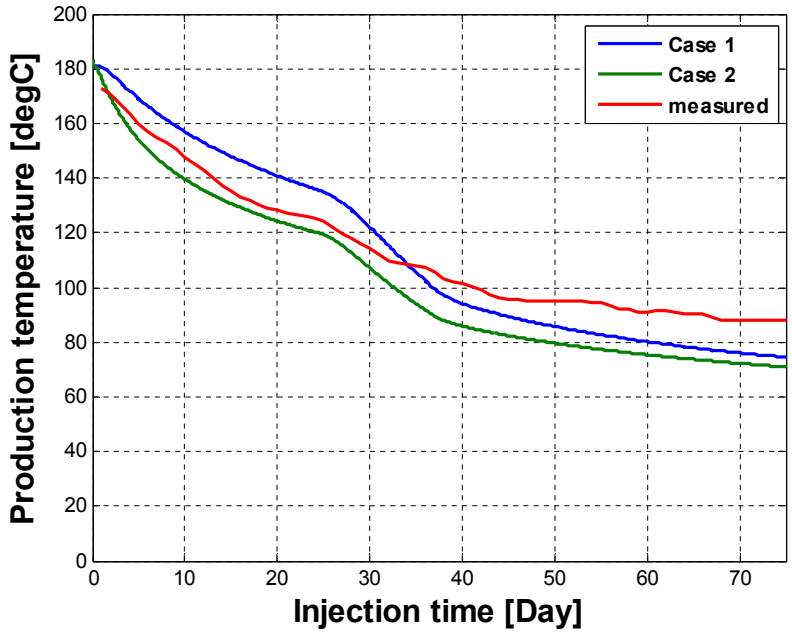

Figure 18: Production temperature versus time for Case 1, Case 2, and the measured data at Fenton Hill

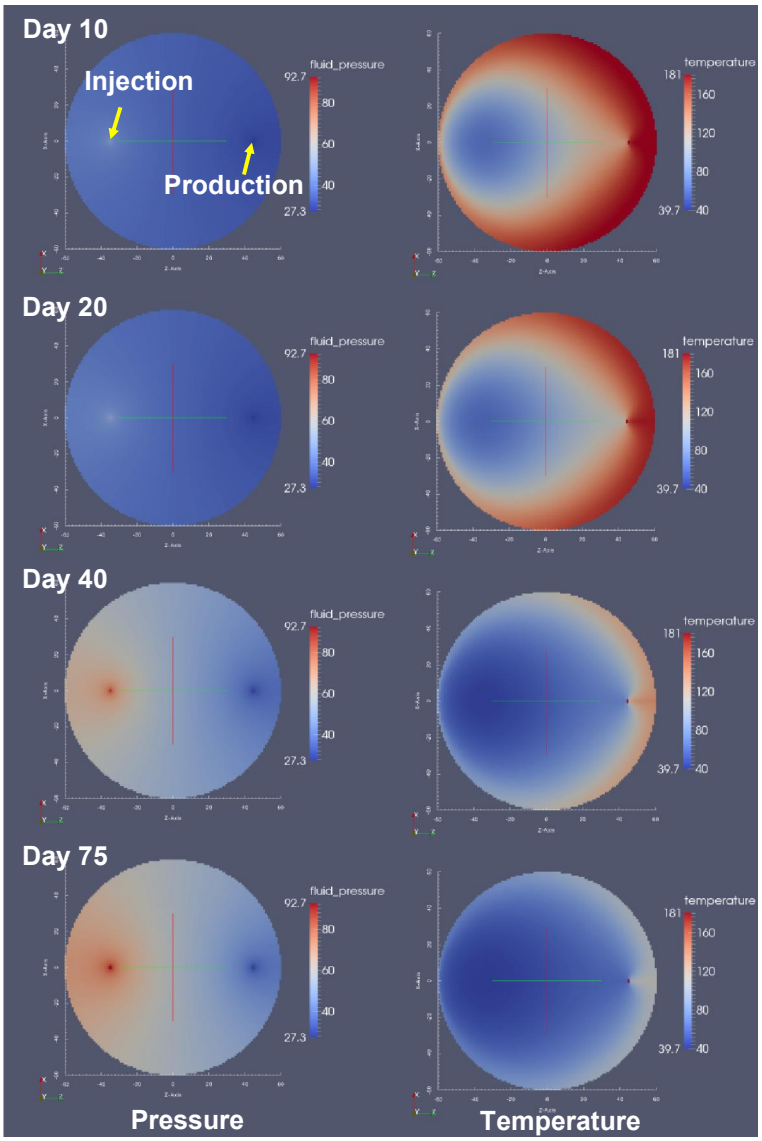

Figure 19: Pressure and temperature distribution across the fracture of Case 1 at days 10, 20, 40, and 75. Locations of the injection and production sites in all the graphs are the same as marked by the yellow arrows in the upper left graph.

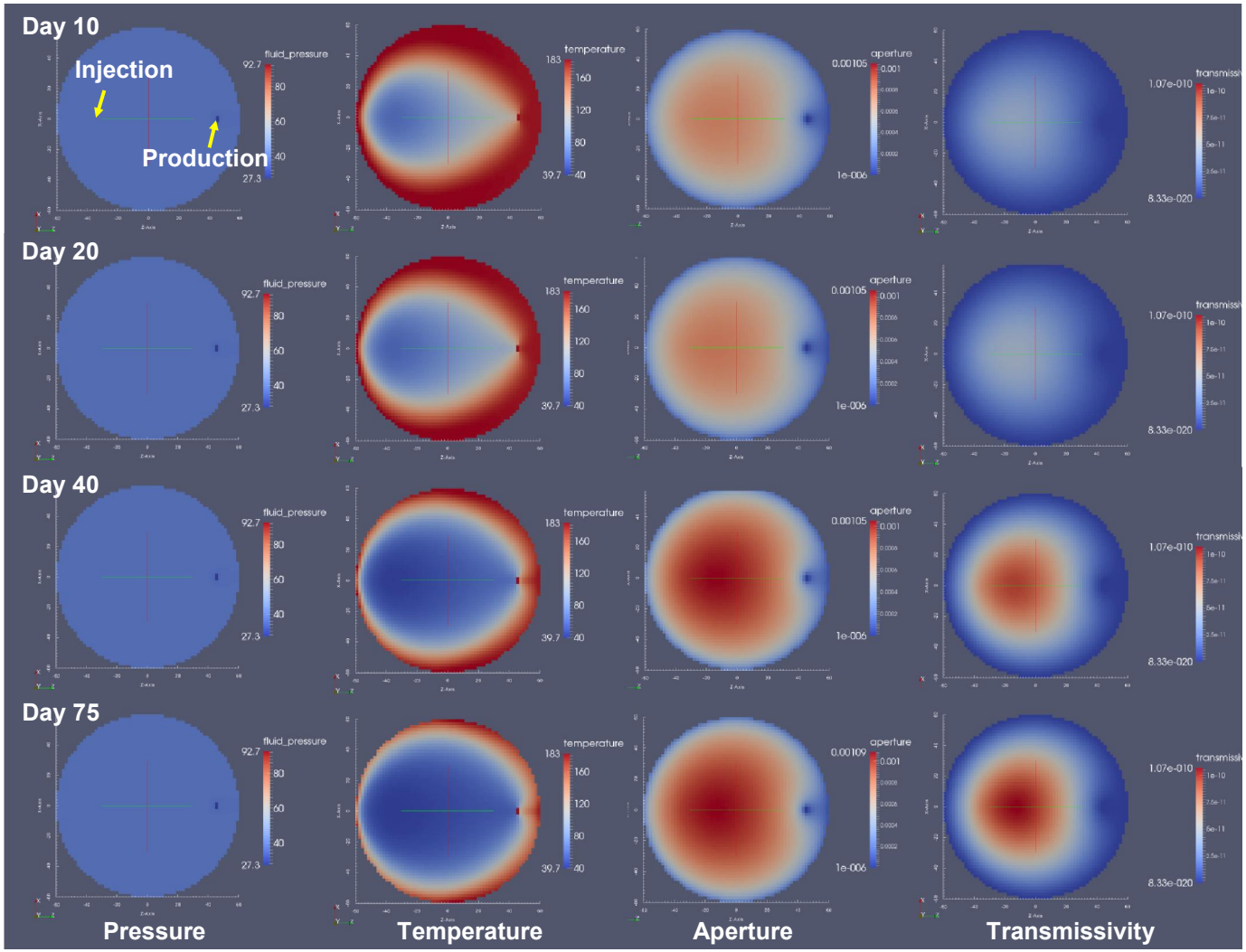

Figure 20: Pressure, temperature, aperture, and transmissivity distribution across the fracture of Case 2 at days 10, 20, 40, and 75. Locations of the injection and production sites in all the graphs are the same as marked by the yellow arrows in the upper left graph.

5.6 REMARKS

For the production temperature series (**Figure 18**), Case 2 is a closer match to the measured data during the first 24 days. After the flow rate is doubled, both Case 1 and Case 2 underestimate the production temperature. At the end of injection, Case 1 has higher production temperature due to a larger sweep area than in Case 2. The heat sweep is less efficient in Case 2 because the aperture and conductivity taper to zero towards the crack tips, unlike Case 1, where aperture is uniform.

For the injection pressure time series (**Figure 17**), the Case 1 pressure increases steadily from day 1 to day 24. This is due to the increasing viscosity of the fluid in the fracture as cooling gradually occurs. From day 25 to day 35, the pressure increases strongly due to the doubling of flow rate. After day 36, the rising of pressure continues, but much more gradually. The Case 2 pressure remains nearly constant. As mentioned in section **5.1**, once the fluid pressure exceeds the normal stress of a particular element on the fracture, that element opens. The cubic law allows fracture transmissivity to increase strongly with only modest increases in aperture. Therefore, the increase in injection rate causes a modest increase in aperture (**Figure 20**), and there is a consequent increase in fracture conductivity, leading to a very modest increase in injection pressure (eq. 2.4).

Chapter 6: Benchmark Problem 6

6.1 PROBLEM OVERVIEW AND DESCRIPTION

This problem is a two-dimensional plane strain case that illustrates the role of coupled thermo-poroelastic processes in natural fracture deformation caused by fluid injection. Water is injected from a well located at the fracture center. With a given fracture geometry and in-situ stresses, time series of pressure, fracture aperture, and shear displacement at the injection wellbore are simulated. Spatial distributions of normal and shear stresses along two specific lines are also observed in this study. In the current stage, since thermal stress has not been implemented into CFRAC, we can only handle this problem isothermally, neglecting the thermoelastic stress. We also neglect poroelastic stresses.

6.2 SYSTEM CONFIGURATION

The vertical fracture shown in **Figure 21** is 40 m long, oriented at 45 degrees in the x-y plane. The injection well is located at the center of the fracture. The maximum and minimum horizontal stresses are 20 MPa and 13 MPa in the y-direction and the x-direction, respectively. Water of 400 K temperature is injected into a 420 K reservoir for 180 days at the flow rate of $6 \cdot 10^{-5}$ kg/s.

The problem description requires using the Barton-Bandis joint mechanical deformation model (Lee and Ghassemi 2011) (eq. 6.1) for calculating the fracture aperture, where σ' is the effective stress, K is the joint stiffness, E_0 is the aperture at zero effective stress, and D is the joint closure defined as E_0 - $E(\sigma')$ and $E(\sigma')$ is the fracture aperture. However, the aperture calculation in CFRAC follows the Willis-Richards model (Willis-Richards et al. 1996) given in equation (2.8). In order to adapt both models, the Barton-Bandis model (eq. 6.1) is first rearranged into equation (6.2), then equation (2.8)

and (6.2) are combined as equation (6.3) to find the relationship between K and σ_{ref} (eq. 6.4). Using the given values, the reference closure stress (σ_{ref}) is set to 13.5 MPa in CFRAC.

$$\sigma' = \frac{KD}{1 - D/E_0}, \tag{6.1}$$

$$E = \frac{E_0}{1 + \sigma'/KE_0}, \tag{6.2}$$

$$\frac{E_0}{1 + 9\sigma'/\sigma_{ref}} = \frac{E_0}{1 + \sigma'/KE_0}, \tag{6.3}$$

and

$$\sigma_{ref} = 9E_0K = 9 \cdot 0.003[m] \cdot 500[MPa/m] = 13.5\ [MPa]. \tag{6.4}$$

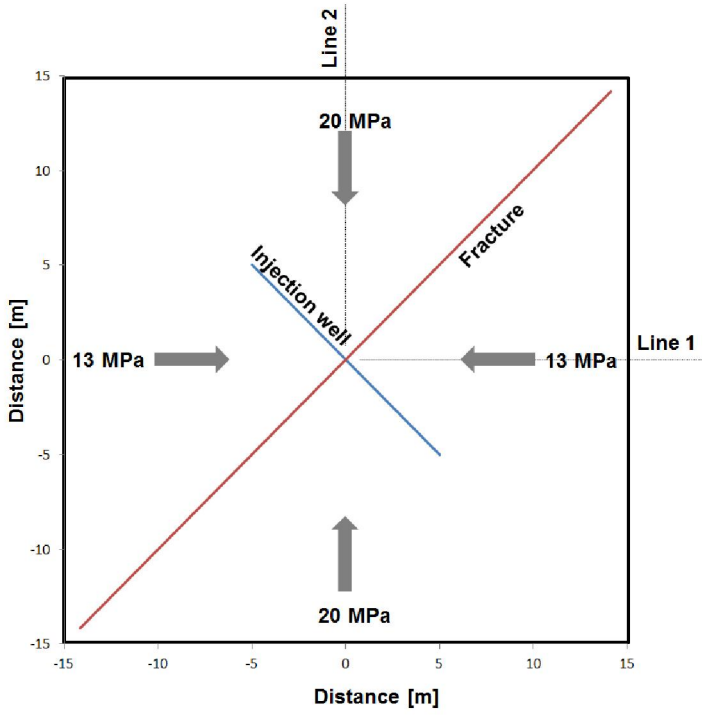

Figure 21: Fracture geometry

6.3 INPUT PARAMETERS

Simulation parameters are given in **Error! Not a valid bookmark self-reference.**. Thermal properties are ignored because our simulations are isothermal.

Table 7: Input properties of Problem 6

Parameter	Value	Unit
Initial pore pressure	10	MPa
Reservoir temperature	420	K
Porosity	0.01	
Permeability	$4 \cdot 10^{-19}$	m^2
Thickness	1	m
Injection flow rate	$0.6 \cdot 10^{-4}$	kg/s
Injection temperature	400	K
Rock density	2480	$kg \cdot m^{-3}$
Fluid compressibility	$4.2 \cdot 10^{-4}$	MPa^{-1}
Water viscosity	$2.037 \cdot 10^{-4}$	Pa·s
Shear modulus	15	GPa
Poisson's ratio	0.25	
Compressive stress in x-dir.	13	MPa
Compressive stress in y-dir.	20	MPa
Initial normal stress on the fracture	16.5	MPa
Initial shear stress on the fracture	3.5	MPa
Simulation duration	180	day
Void aperture reference value, E_0	0.003	m
Reference closure stress, σ_{ref}	13.5	MPa

6.4 METRICS

Several time series at the wellbore and spatial distribution plots of aperture, shear displacement, and normal and shear stresses along specific lines should be provided (**Error! Not a valid bookmark self-reference.**).

Table 8: Result metrics of Problem 6

Metric	Parameter	Locations (x, y) [m]	Time
Time series	*Pressure*	(0, 0), at the wellbore	180 days, continuous
	Aperture		
	Shear displacement		
Spatial distribution	*Aperture*	x = y, along the fracture	At days 5, 75, and 180
	Shear displacement		
	Normal stress	Line 1 (**Figure 21**)	Day 180
	Shear stress	Line 2 (**Figure 21**)	

6.5 RESULTS

Time series of pressure, aperture, and shear displacement are shown in **Figure 22** and **Figure 23**. The pressure starts from the initial fluid pressure of 10 MPa, and does not exceed 18 MPa by the end of injection. The aperture and shear displacement increase continuously during the water injection. The maximum aperture and shear displacement are 3.42 and 6.86 mm after 180 days of injection. The spatial distribution plots of aperture and shear displacement are shown in **Figure 24** and **Figure 25**. The maximum values always occur at the center of the fracture. The normal and shear stresses along Line 1 and Line 2 are shown in **Figure 26** and **Figure 27**, respectively. Notice that the normal stress for Line 1 is in the y-direction whereas normal stress for Line 2 is in the x-direction.

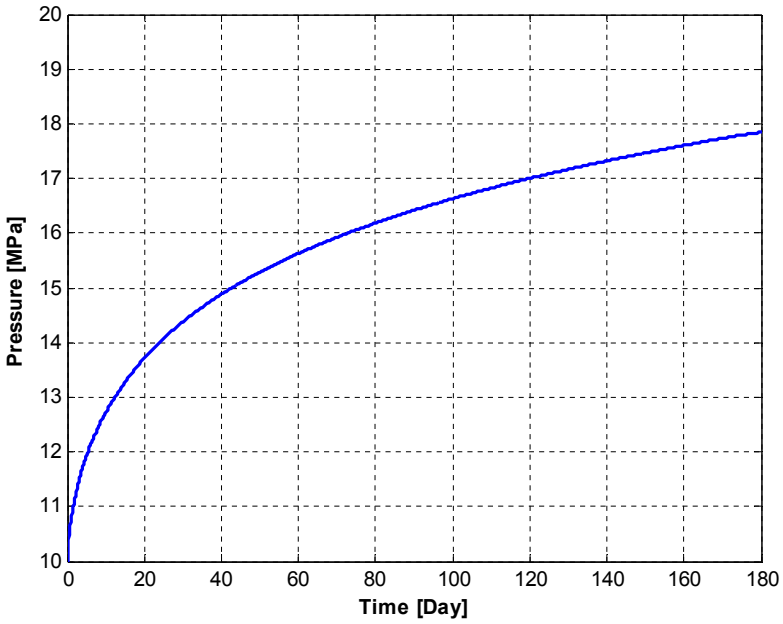

Figure 22: Pressure as a function of time at the wellbore

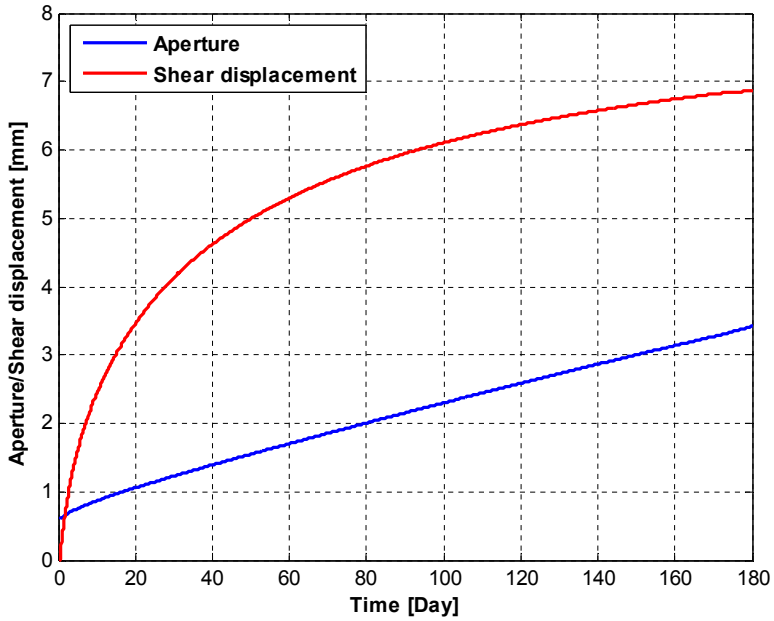

Figure 23: Aperture and shear displacement as a function of time at the wellbore

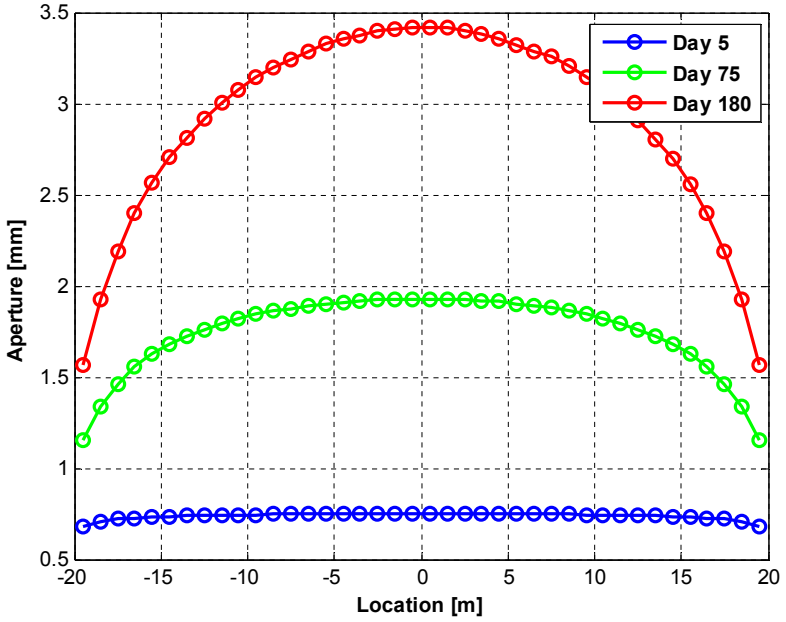

Figure 24: Aperture along the fracture at days 5, 75, and 180

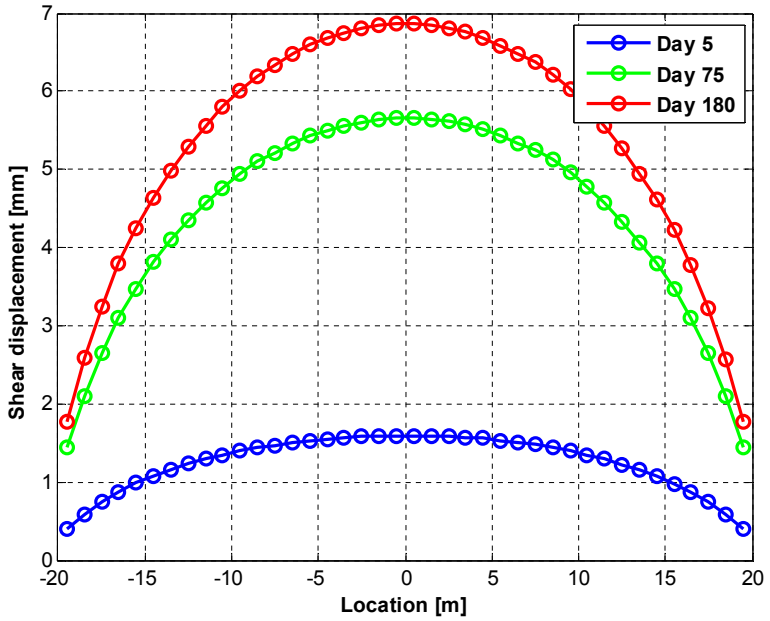

Figure 25: Shear displacement along the fracture at days 5, 75, and 180

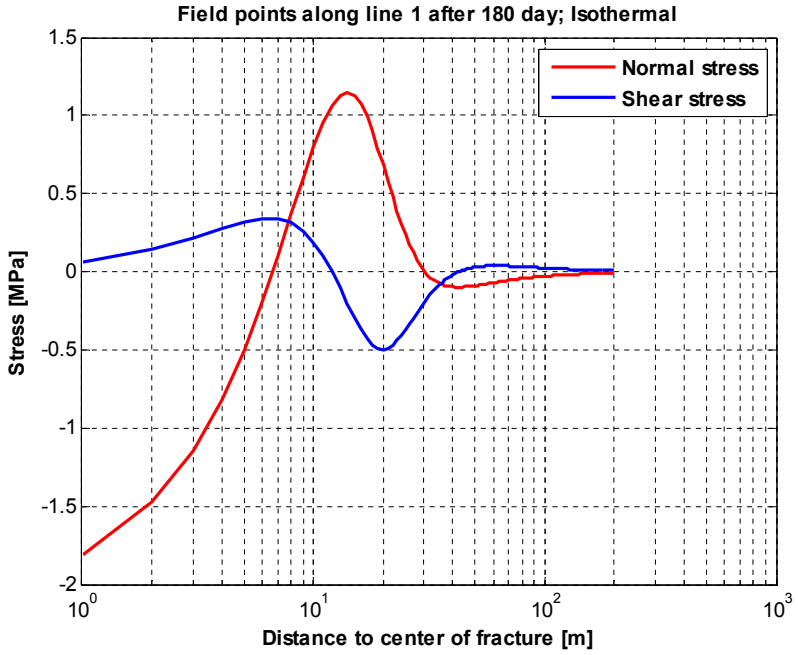

Figure 26: Normal and shear stresses along Line 1 after 180 days

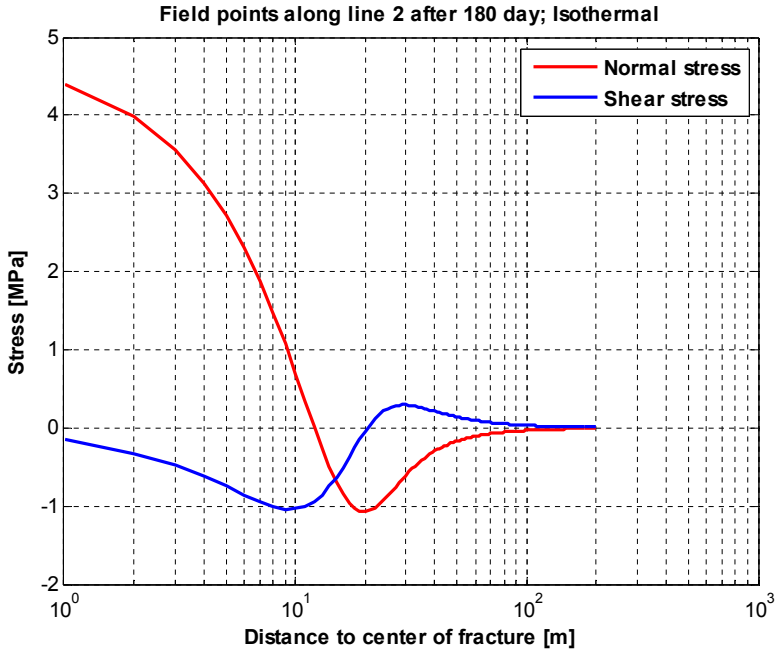

Figure 27: Normal and shear stresses along Line 2 after 180 days

6.6 REMARKS

This problem is dealt with as an isothermal, plane strain, linear elastic fracture. As the fluid pressure increases, both the aperture and the shear displacement increase. Yet, the aperture and shear displacement increase at very different rates. **Figure 23** shows that the aperture increases almost linearly with time, while the shear displacement increases rapidly in the beginning and slows down later. The same scenario can be observed in **Figure 24** and **Figure 25** as well. Moreover, our shear displacement increases to 6.86 mm after 180 days of injection. This shear displacement occurs because the fluid pressure exceeds the normal stress and causes a complete friction loss on the fracture walls. However, the fluid pressure does not exceed the normal stress everywhere along the fracture, as shown in **Figure 24**, where aperture remains below E_0 at the outer parts of the fracture, even after 180 days.

The stress in this region is strongly affected by the opening and shearing of the fracture, partially near the fracture tip area. In **Figure 26** and **Figure 27**, the normal and shear stresses in different locations are in different corresponding directions. Therefore, it is inappropriate to compare stresses on Line 1 and Line 2 side by side directly. Clearly, as Line 1 and Line 2 move away from the fracture, the stress influenced by the fracture becomes smaller.

Chapter 7: Benchmark Problem 7

7.1 PROBLEM OVERVIEW AND DESCRIPTION

The objective of Problem 7 is to quantify the surface vertical displacement in response to water injection into a subsurface fracture. The effect of the surface vertical displacement is particularly significant because the fracture is shallow. In this problem, the center of the fracture is only 125 m in depth, which might be too shallow in general EGS, but the purpose of this benchmark problem is simply for testing. Three assumptions are adopted: (1) the medium is isotropic and homogeneous; (2) the fracture has uniform pressure internal pressure; (3) the fracture is rectangular. Various dipping angles are considered: 0^0, 45^0, and 90^0. Participating teams can choose to solve this problem by two- or three-dimensional simulation. Due to the constraints of CFRAC, we only submit the result of a 90^0 dipping fracture in a three-dimensional simulation. Additionally, the stress intensity factor along the upper and lower fracture edges is calculated.

7.2 SYSTEM CONFIGURATION

As shown in **Figure 28a**, two coordinate systems are established to describe the spatial relationships. The origin of the global coordinate system (x-y-z) is at the projection of the fracture center onto the surface. The origin of the local coordinate system (u-v) is located at the fracture center. The length and width of the fracture are *2b* and *2a*, and the dipping angle is β. Based on these settings, the fracture center is set at (0, -*d*, 0) in the global coordinate system where -*d* is the depth and (0, 0) in the local coordinate system of the fracture plane. The only case simulated by our team for this problem is for $\beta = 90^0$. The fracture cross section in the particular setting is shown in **Figure 28b**.

The displacement of the ground surface is calculated by boundary element method, and the medium is considered as semi-infinite. The results of displacement are normalized

by the maximum normal displacement from the 2D problem (δ_∞) given by Pollard and Holzhausen (1979) as equation (7.1):

$$\delta_\infty = P_0 \cdot a \cdot \frac{(1-\nu)}{G}, \tag{7.1}$$

where P_0 is the fluid pressure, a here is the half width (or half height in the $\beta = 90^0$ case) of the fracture, G is the shear modulus, and v is Poisson's ratio.

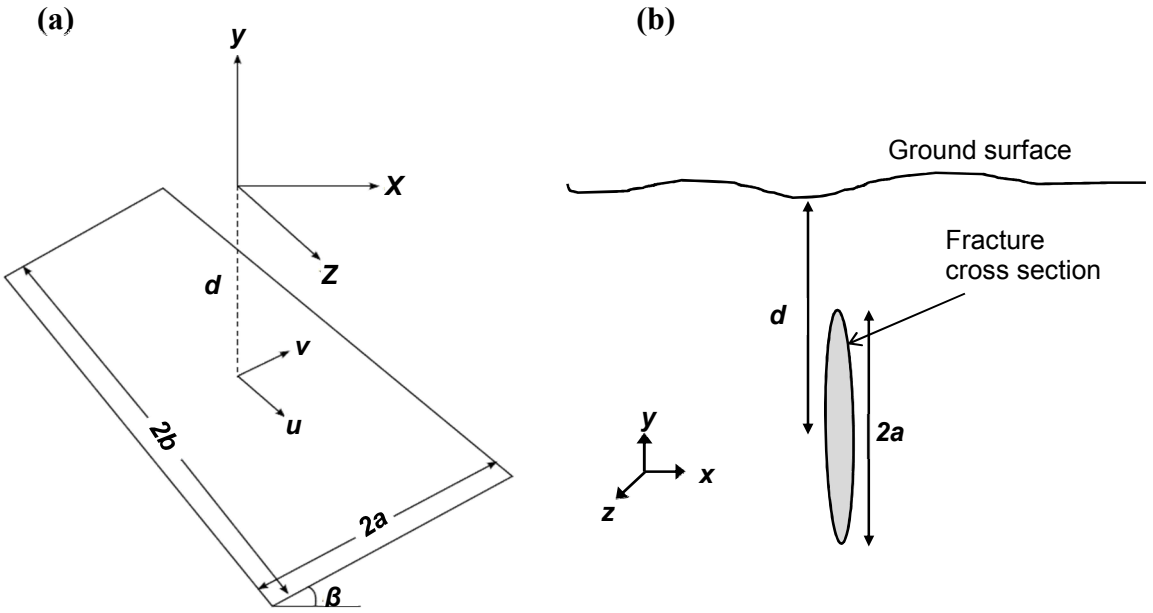

Figure 28: **(a)** Fracture geometry and coordinate systems on the fracture (u-v) and the surface (x-y-z) (Bahrami et al. 2015) **(b)** fracture cross section when $\beta = 90^0$

The stress intensity factor is calculated using the equation given by Olson (2007) as equation (7.2), where K_I is the mode-I stress intensity factor, G is the shear modulus, v is Poisson's ratio, a_h is the minimum of element half-length or half-height, and E_{open} is the separation amount of the fracture walls during opening (McClure et al. 2015). Same as the

surface displacement, the stress intensity is normalized using the maximum mode-I intensity factor from the 2D problem (K_0) given by Pollard and Holzhausen (1979), shown in equation (7.3).

$$K_I = 0.806\left[\frac{2G\sqrt{\pi}}{4(1-\nu)\sqrt{a_h}}\right]E_{open}, \tag{7.2}$$

and

$$K_0 = P_0\sqrt{\pi a}\,. \tag{7.3}$$

7.3 INPUT PARAMETERS

Properties from the problem description and some of the CFRAC settings are listed in **Table 9**.

Table 9: Input properties of Problem 7

Parameter	Value	Unit
Fracture dimension, a	100	m
Fracture dimension, b	300	m
Depth, d	125	m
Fracture dipping, β	90	degree
Shear modulus, G	4	GPa
Poisson's ratio, v	0.25	
Compressive stress in x-dir.	20	MPa
Compressive stress in y-dir.	20	MPa
Max. injection pressure	21	MPa

7.4 METRICS

Metrics reported in this problem are: (1) surface vertical displacement data along the x-axis from x = -4*a* to x = 4*a* and z-axis from z = -4*b* to z = 4*b* in the global coordination system, and (2) mode-I stress intensity factor along the fracture edge where v = *a* in the local fracture coordination system. In our case, when the fracture's dipping angle is 90^0, the upper edge of the fracture is v = *a*. For further comparison, the stress intensity factor of the lower edge where v = -*a* is also presented. The complete result metrics are shown in **Table 10**.

Table 10: Result metrics of Problem 7

Metric	Parameter	Location	Time [s]
Spatial distribution	*Surface displacement*	x = -4*a* to x = 4*a,* x-axis	100000
		z = -4*b* to z = 4*b,* z-axis	
	Mode-I stress intensity factor	v = *a*, upper edge	
		v = - *a*, lower edge	

7.5 RESULTS

The three-dimensional surface vertical displacement mesh is shown in **Figure 29**. The cross sections of normalized vertical displacement along x-axis and z-axis are shown in **Figure 30**, which shows that the most subsidence is just right above the fracture and the maximum vertical displacement occurs in both sides of the fracture within the range of half the fracture width. The mode- I stress intensity factor distributions of the upper and lower edges along the fracture are presented in **Figure 31** where the values of the upper edge are always larger than the lower ones.

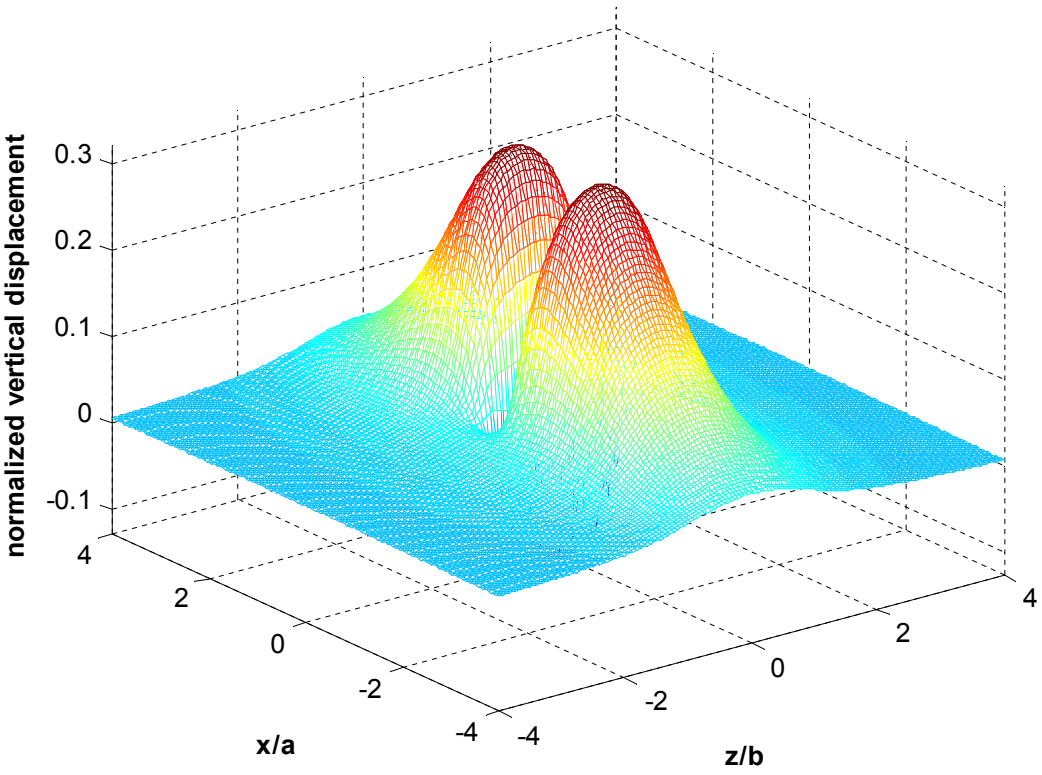

Figure 29: Surface vertical displacement mesh

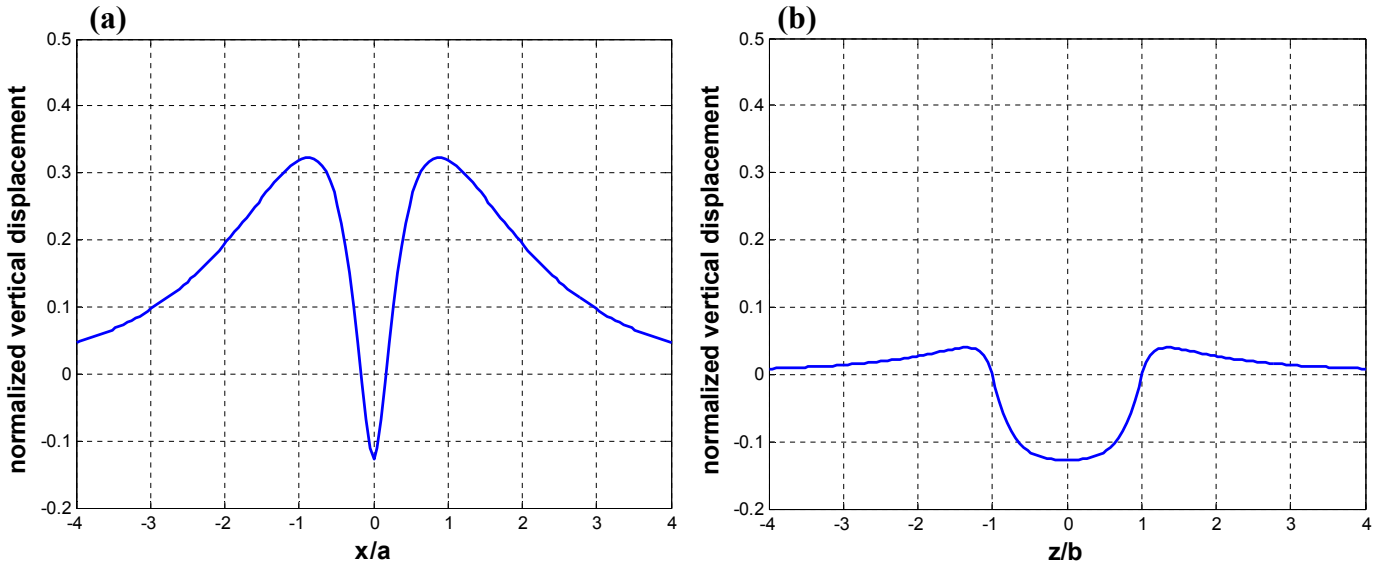

Figure 30: Surface vertical displacement along **(a)** x-axis and **(b)** z-axis

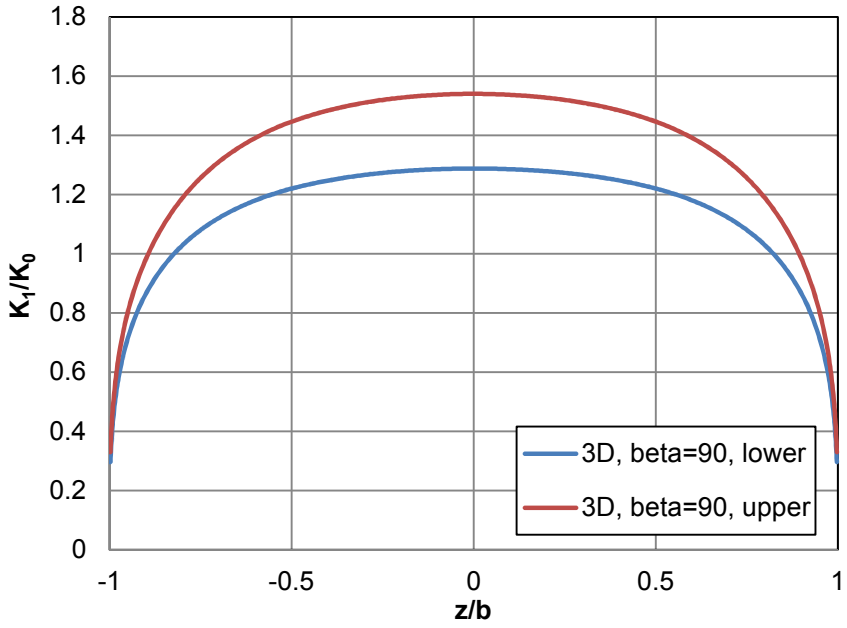

Figure 31: Stress intensity factor of the lower and upper edges of the vertical fracture

7.6 REMARKS

In CFRAC, the displacement of the ground surface is calculated by the boundary element method (BEM) (McClure et al. 2015). The testing fracture in Problem 7 is a good candidate for calculating the vertical ground displacement because the depth of the fracture upper edge is only 25 m from the ground surface. Our results, shown in **Figure 30**, closely agree with the results submitted by other participating teams (Bahrami et al. 2015), in both x and z directions. Along the x-axis, the subsidence locates at x = 0, right above the fracture, and the ground surface on both sides of the fracture around $x = \pm 0.85a$ is being lifted. For the cross section along the z-axis, the ground also subsides above the fracture from $z = -b$ to b, and a relatively minor increase in elevation is generated at $z = \pm 1.33b$, out of the projection range of the fracture. Eventually, if we plot the cross section far enough, the displacement in the far-field goes to zero in either the x or z direction.

Stress intensity factor is an important concept in fracture mechanics, especially for fracture propagation. The fracture propagates when the stress intensity factor is greater than the fracture toughness (McClure et al. 2015).

Chapter 8: Conclusion

The first stage of this GTO-CCS study concluded at the end of 2014. Our results of Benchmark Problems 1, 2, 4, 6, and 7 are presented in this report. Problem 1, 6, and 7 are solved as single fracture H-M cases, and Problem 2 and 4 are T-H-M cases. This project overall confirms that CFRAC can handle EGS problems coupling thermal, hydrologic, and geomechanical processes with given reservoir conditions, fracture settings, and appropriate assumptions. Physical characteristics, including fluid pressure, permeability, fracture deformation, flow rate, and temerature distribution, can be calculated and provide a clearer picture of processes in geothermal reservoirs.

In the current version of CFRAC, poroelasticity and thermoelasticity, using a point source for injection, and arbitrary fracture dipping angle cannot be modeled. However, in spite of these limitations, reasonable results can still be obtained for a wide range of EGS and hydraulic fracturing problems by applying minor modifications and adjustments. In the future, simulations of more complicated three-dimensional fracture networks with multiple wells will be developed and tested as preparation for the second stage of the GTO-CCS study, which will involve matching a field-scale EGS dataset.

References

Bahrami, D., Danko, G., Fu, P., Guo, B., Podgorney, R., White, M., and Xia, Yidong. 2015. Poroelastic and self-propped single fracture THM models for EGS studies. *Proceedings of the 40th Workshop on Geothermal Reservoir Engineering*, Stanford, California, USA, January 26-28.

Deb, R. and Jenny, P. 2015. Numerical modeling of flow induced shear failure in fractured reservoirs. *Proceedings of the 40th Workshop on Geothermal Reservoir Engineering*, Stanford, California, USA, January 26-28.

Ghassemi, A., Kelkar, S. and McClure, M. 2015. Influence of fracture shearing on fluid flow and thermal behavior of an EGS reservoir - Geothermal code comparison study. *Proceedings of the 40th Workshop on Geothermal Reservoir Engineering*, Stanford, California, USA, January 26-28.

Lee, B. T. and Ghassemi, A. 2011. Shear slip and permeability change caused by injection/ extraction in a fractured reservoir. In *45th US Rock Mechanics/Geomechanics Symposium*, San Francisco, California, USA, June 26-29.

Lemmon, E.W., McLinden, M.O., and Friend, D.G. Thermophysical properties of fluid systems. *NIST Chemistry WebBook, NIST Standard Reference Database.* no. 69, Eds. Linstrom, P.J. and Mallard, W.G. *National Institute of Standards and Technology*, Gaithersburg, MD, 20899, http://webbook.nist.gov, (retrieved March 23, 2015).

McClure, M. W. 2012. Modeling and characterization of hydraulic stimulation and induced seismicity in geothermal and shale gas reservoirs. PhD diss., Stanford University.

McClure, M. W. 2014a. Stimulation mechanism and the direction of propagation of microseismicity. *Proceedings of the 39th Workshop on Geothermal Reservoir Engineering*, Stanford, California, USA, February 24-26.

McClure, M. W. 2014b. The potential effect of network complexity on recovery of injected fluid following hydraulic fracturing. *SPE Unconventional Resources Conference*, The Woodlands, Texas, USA, April 1-3.

McClure, M. W., Babazadeh, M., Shiozawa, S., and Huang, J. 2015. Fully coupled hydromechanical stimulation of hydraulic fracturing in three-dimensional discrete fracture networks. *SPE Hydraulic Fracturing Technology Conference*, The Woodlands, Texas, USA, February 3-5.

McClure, M. W. and Horne, R. N. 2010. Discrete fracture modeling of hydraulic stimulation in enhanced geothermal systems, *Proceedings of the 35th Workshop on Geothermal Reservoir Engineering*, Stanford, California, USA, February 1-3.

McClure, M. W. and Horne, R. N. 2013. Discrete fracture network modeling of hydraulic stimulation coupling flow and geomechanics. *Springer Science & Business Media*.

McClure, M. W. and Horne, R. N. 2014a. Characterizing hydraulic fracturing with a tendency for shear stimulation test. *SPE Reservoir Evaluation & Engineering,* v. 17, no. 2, pp. 233-243.

McClure, M. W. and Horne, R. N. 2014b. CFRAC (version 1.2) complex fracturing research code user's guide (version 20).

Murphy, H. D., Tester, J. W., Grigsby C. O., and Potter, R. M. 1981. Energy extraction from fractured geothermal reservoirs in low-permeability crystalline rock. *Journal of Geophysical Research: Solid Earth*, v. 86, no. B8, pp. 7145-7158.

Nathenson, M. 1999. The dependence of permeability on effective stress from flow tests at hot dry rock reservoirs at Rosemanowes (Cornwall) and Fenton Hill (New Mexico). *Geothermics,* v. 28, no. 3, pp. 315-340.

Norbeck, J. and Horne, R. 2015. Injection-triggered seismicity: an investigation of porothermoelastic effects using a rate-and-state earthquake model. *Proceedings of the 40th Workshop on Geothermal Reservoir Engineering*, Stanford, California, USA, January 26-28.

Olson, J. E. 2007. Fracture aperture, length and pattern geometry development under biaxial loading a numerical study with applications to natural, cross-jointed systems. *Geological Society*, London, Special Publications, v. 289, no. 1, pp. 123-142.

Pollard, D. D. and Holzhausen, G. 1979. On the mechanical interaction between a fluid-filled fracture and the earth's surface. *Tectonophysics*, v. 53, no. 1, pp. 27-57.

Rice, J. R. 1993. Spatio-temporal complexity of slip on a fault. *Journal of Geophysical Research,* v. 98, no. B6, pp.9885-9907.

U.S. Department of Energy. 2008. An Evaluation of enhanced geothermal systems technology. *EERE*, *Geothermal Technologies Program.*

Vinsome, P. and Westerveld, J. 1980. A simple method for predicting cap and base rock heat losses in thermal reservoir simulators. *Journal of Canadian Petroleum Technology*, v. 19, no. 3, pp. 87-90.

White, M. D. and Phillips, B. R. 2015. Code comparison study fosters confidence in the numerical simulation of enhanced geothermal systems. *Proceedings of the 40th Workshop on Geothermal Reservoir Engineering*, Stanford, California, USA, January 26-28.

Willis-Richards, J., Watanabe, K., and Takahashi, H. 1996. Progress toward a stochastic rock mechanics model of engineered geothermal systems. *Journal of Geophysical Research*, v. 101, no. B8, pp. 17481-17496.